1986

Work of fracture of sodium chloride single crystals

Bai-Yun Huang
Iowa State University

Huang, Bai-Yun

WORK OF FRACTURE OF SODIUM CHLORIDE SINGLE CRYSTALS

Iowa State University PH.D. 1986

PLEASE NOTE:

In all cases this material has been filmed in the best possible way from the available copy. Problems encountered with this document have been identified here with a check mark __✓__.

1. Glossy photographs or pages ✓
2. Colored illustrations, paper or print _____
3. Photographs with dark background ✓
4. Illustrations are poor copy _____
5. Pages with black marks, not original copy _____
6. Print shows through as there is text on both sides of page _____
7. Indistinct, broken or small print on several pages _____
8. Print exceeds margin requirements _____
9. Tightly bound copy with print lost in spine _____
10. Computer printout pages with indistinct print _____
11. Page(s) _____ lacking when material received, and not available from school or author.
12. Page(s) _____ seem to be missing in numbering only as text follows.
13. Two pages numbered _____. Text follows.
14. Curling and wrinkled pages _____
15. Dissertation contains pages with print at a slant, filmed as received _____
16. Other _____

_____

_____

University
Microfilms
International

Work of fracture of sodium chloride single crystals

by

Bai-Yun Huang

A Dissertation Submitted to the

Graduate Faculty in Partial Fulfillment of the

Requirements for the Degree of

DOCTOR OF PHILOSOPHY

Department: Materials Science and Engineering
Major: Metallurgy

Approved:

Signature was redacted for privacy.

In Charge of Major Work

Signature was redacted for privacy.

For the Major Department

Signature was redacted for privacy.

For the Graduate College

Iowa State University
Ames, Iowa

1986

TABLE OF CONTENTS

	Page
INTRODUCTION	1
REVIEW OF LITERATURE	4
Plastic Deformation and Dislocation Theory	4
Photoelasticity	16
Fracture Mechanics	20
EXPERIMENTAL PROCEDURE	24
Determination of the Burgers Vector	24
Sample Preparation for One Active Slip System	25
Sample Preparation for Fully Stable Fracture	36
Design of Pyrogenic and Cryogenic Systems	45
RESULTS AND DISCUSSION	48
Birefringence in Sodium Chloride Single Crystals	48
Birefringence of the edge dislocation slip line	48
Stress field of the edge dislocation pile up	52
The uniqueness of the dislocation birefringence	59
Plastic zone shape in sodium chloride single crystals	66
Measurement of Work of Fracture	73
Unstable fracture of ductile body	73
Variable parameters of work of fracture	79
Stable fracture of elastic-plastic body	89
CONCLUSIONS	94
BIBLIOGRAPHY	96
ACKNOWLEDGMENTS	100
APPENDIX A. SEMIQUANTITATIVE SPECTROGRAPHIC ANALYSIS OF SODIUM CHLORIDE SINGLE CRYSTALS	101

Page

APPENDIX B. DESIGN OF PYROGENIC SYSTEM 102

Furnace Insulation 102

Power Supply 104

INTRODUCTION

Brittle fracture has occurred in metal structures such as tanks, vessels, ships, bridges, airplanes, etc. [1-3]. This catastrophic failure of metal has caused the loss of a number of lives and has caused economic loss. Many studies have been completed to try to prevent brittle fracture. Such studies include improvement of materials properties, good design, fabrication and so on. All these are based on the understanding of the processes and mechanisms of fracture.

Brittle fracture is also a serious problem for other engineering materials. Ceramic materials are an example. The structural uses of ceramic materials have been primarily limited to situations involving only low levels of static stress, usually compression. This limitation is imposed by the brittle nature of ceramic materials. The need for ductile ceramic has stimulated an intensive research effort [4]. The solution for brittle fracture in ceramic materials is also closely related to the processes and mechanisms of fracture. The purpose of this study is to understand these processes and mechanisms (especially on a microscale).

In order to understand the processes and mechanisms of fracture, sodium chloride single crystals were selected to study in this research. Even though sodium chloride is not a useful structure material, it has advantages for studying fracture mechanisms.

First, it is transparent. Therefore, photoelastic analysis can be used to observe the plastic deformation at the crack tip, i.e.,

dislocation slip planes at the crack tip can be observed.

Second, it is available in the form of large single crystals. As will be explained later, for three- or four-point bending, the size of the sample was about 8 x 14 x 50 mm. To avoid property changes from ingot to ingot, all samples were taken from a single crystal ingot. Therefore, a very large ingot of single crystals was needed. To study the relationship between the birefringence and dislocation slip, large single crystals were also necessary. In comparison with many other materials, large single crystals of sodium chloride are easily available, and they are also economical.

Finally, sodium chloride has a typical face center cubic structure. This structure appears in many metallic and ceramic materials. The atomistic processes of plastic deformation in sodium chloride have been shown to be similar to many other materials. Therefore, sodium chloride can be taken as a good model to study deformation, fracture, and their dislocation mechanisms.

Everything has two sides: advantages and disadvantages. The disadvantage for sodium chloride in this research is that it is not available in polycrystalline form. In bending tests on single crystals, the fracture toughness parameters are dependent on the sample size, due to plastic deformation developed far away from the tip of the notch. In other words, different sample sizes will absorb different plastic deformation energy for a given crack propagation. Polycrystals can avoid this situation because the grain boundaries of polycrystals can limit the length of the dislocation slip line. Once the dislocation

slip can be stopped, plastic deformation will be limited in a small region at the tip of the crack. Therefore, sample size effects on the plastic deformation energy will be reduced. Polycrystals are needed in this case, but they are not available in sodium chloride. Despite this disadvantage, from the experimental point of view, the ability to study plastic deformation by photoelastic methods makes sodium chloride especially valuable for studying fracture mechanisms.

REVIEW OF LITERATURE

Plastic Deformation and Dislocation Theory

In the nineteenth century, slip bands were first observed [5]. These bands were interpreted as being the result of plastic deformation. The actual values of the shear stress required to produce this plastic deformation in metal single crystals are much smaller than the theoretical shear strength. According to the theoretical calculation of perfect crystal, the theoretical shear stress, τ_{th}, is

$$\tau_{th} = \frac{b}{a} \frac{G}{2\pi} \tag{1}$$

where

G = shear modulus,

b = spacing between atoms in the direction of the shear stress and

a = spacing of the rows of atoms.

Since $a \approx b$, the τ_{th} is about $1/2\pi$ G. Actual values of the shear stress required to produce plastic deformation are 10^{-4} - 10^{-6} G [6]. Therefore, there is quite a difference. The solution of the apparent contradiction above was proposed by Orowan [7], Polanyi [8] and Taylor [9], and the concept of a dislocation was introduced.

Some basic concepts of dislocation established earlier can be described as follows:

(1) Dislocation line - Cut a perfect crystal lattice part way through along any of the planes. The trace of the cut in the lattice is a line. Let the atoms on one side of the cut shift in a direction parallel to the cut surface through a distance equal to one atom spacing. Then, rejoin the atoms on either side of the cut. Thus, the trace of the cut line in the lattice is not perfect. This line is called the dislocation line.

(2) Burgers circuit and Burgers vector - A Burgers circuit is any atom to atom path taken in a crystal which forms a loop. If the atom to atom sequence is made in a perfect crystal, the Burgers circuit will close. If the atom to atom sequence is made in a crystal containing dislocations, the Burgers circuit does not close and it must enclose one or more dislocations. The vector required to complete the circuit is called the Burgers vector.

(3) Edge dislocation and screw dislocation - If the Burgers vector of a dislocation is normal to the line of the dislocation, this dislocation is called an edge dislocation. If the Burgers vector of a dislocation is parallel to the line of the dislocation, this dislocation is a screw dislocation.

The dislocations in crystals changed the plastic behavior of the crystals. The plastic deformation in crystals is conducted by the dislocation slip. The stress that is required to move a dislocation is much smaller than the theoretical shear stress of a perfect lattice. This stress required to move a dislocation has been calculated by Peierls [10] and Nabarro [11]. It was called Peierls force or

Peierls-Nabarro force.

Although the concept of a dislocation began much earlier, the study of dislocations, both theoretical and experimental, was developed mainly after World War II [12]. Since then, the presence of dislocations was known to alter not only the plastic properties of crystals, but also a large number of other properties, such as crystal growth rate, electrical properties of semiconductors, magnetic hardness, superconductive properties and so on. The classical treatises by Read [13] and Cottrell [14] were the distinguishing marks of the development of dislocation theory. As Friedel [12] said in 1964, "If the possible fields of application are still wide open, the 'theory' of the dislocation might be considered as nearly completed."

With the development of dislocation theory, many attempts to observe the dislocation were made successfully. These observations helped to understand plastic deformation. In the general case, the dislocation slip is a main mechanism of plastic deformation in materials which possess many possible slip systems. Twinning also allows plastic deformation, but it is not a dominant deformation mechanism [15], except when dislocation movement is difficult at low temperature [16]. In other words, plastic deformation is closely related to dislocation movement. Dislocation phenomena are the basis of the plastic deformation and micromechanisms of fracture.

Six common methods of dislocation observation are often used. They are reviewed below.

(1) Etching - This method consists simply in immersing the crystal in a suitable medium, e.g., a solution. It is found that small pits are developed at the emergence points of dislocations. The shape of the etch pit depends on the character of the dislocation. It is sometimes possible to distinguish between edge and screw dislocation [17] and between positive and negative edge dislocations [18]. The etching technique can also be used to study the movement of dislocation, as demonstrated by Gilman et al. (as cited in Reference [19]). Different methods of etching are used: chemical etching, solution etching, preferential oxidation, electrolytic etching, cathodic sputtering and so on. The most common method is chemical etching. Some etchants for revealing dislocation in NaCl are listed in Table 1 [20].

Table 1. Etchants for revealing dislocations in NaCl[a]

Etchant	Source
$MgCl_2$ in ethanol	Moran
$FeCl_3$ in acetic acid	Mendelson
Methanol and acetic acid	Davidge and Whitworth
$MgCl_2$ in acetic acid	Long
$MnCl_2$ in ethanol	Long
$PbCl_2$ in water	Long

[a]From Reference [20].

(2) Decoration method - Some crystals are transparent to light and infrared radiation. It is possible to decorate the dislocations by inducing precipitation along the line of the dislocation [21, 22]. For example, KCl crystals were heavily doped by the addition of 0.75 percent of AgCl to the melt prior to growth of the crystals. The crystals were annealed in a stream of hydrogen between 650°C and 700°C for 3 hrs. Particles of Ag were precipitated on the dislocations in the region of the crystal immediately below the surface. Therefore, the dislocation can be found by the precipitated particles of Ag.

(3) Transmission electron microscopy - Transmission electron microscopy has been used to study dislocations, stacking faults, twin and grain boundaries in a wide variety of materials which can be produced in very thin sections [23]. There are three methods for using transmission microscopy to observe the dislocation as follows.

(a) Molecular crystals - When crystals with lattice spacings greater than the TEM resolution are studied, it is possible to observe dislocations directly. J. W. Menter [24] has made such observations on thin crystals of copper and platinum phthalocyanine, in which the spacing of atom planes is about 12 A°. It is proposed that the image lines on the screen of TEM can be regarded in first approximation as a projection of the sheets of molecules. Dislocation can be seen by the imperfection of the image lines.

(b) Moiré fringes - In metals, the spacing between atom planes is about 0.2 nm and therefore, less than the resolution of the

electron microscope. The Moiré fringes were used to produce an effective magnification of this spacing. When two parallel sets of lines, with spacing d_1 and d_2, are superimposed, an enlarged pattern of parallel fringes is produced with a spacing $(d_1 \cdot d_2)/(d_2-d_1)$ giving a Moiré magnification $d_1/(d_2-d_1)$. In an analogous way, dislocation can be revealed by superimposing two crystals with the same crystal structure, but different lattice parameters. Bassett, Menter and Pashley deposited a layer of palladium onto a (111) gold film giving a Moiré magnification of ~20 and observed the dislocations by the image distortion (from reference [25]).

(c) General application - The molecular crystal method requires large spacing of atom planes. The Moiré fringes method requires a difficult specimen preparation. Both methods have a very limited application. The third method is the "diffraction pattern." The mechanism of forming the image of the diffracted beam is as follows. A parallel electron beam is transmitted through a sample and is diffracted in a number of directions by the crystal. The diffracted beams are brought to a focus in the back focal plane of the objective lens, thus forming a diffraction pattern. The diffraction pattern in the focus plane consists of an approximately two-dimensional array of spots, each spot corresponding to a particular set of reflecting planes. The beam which is not diffracted is the transmitted beam. Each beam can form an image in the image plane and it can be magnified by other lenses in the instrument. The image resulting from a single beam can

be obtained by inserting an objective aperture. If transmitted beam is selected, it is a bright field image. If any single diffracted beam is selected, it is a dark field image [26]. Both can be used to observe the dislocations on the screen.

(4) Scanning electron microscopy - There are two methods to observe the dislocations in SEM.

(a) Electron channeling patterns - The electron channeling pattern (ECP) can provide crystal orientation and crystal perfection information [27, 28]. In crystals, the atomic packing density differs along different crystallographic directions. At certain angles of incidence, the electrons will be moving parallel to the crystalline lattice planes. In such cases, the packing density of atoms will appear to be reduced because they are all lined up. The electrons penetrate more deeply into the crystal, passing between the rows of atoms along "channels", and consequently, the backscattering production coefficient, η, will fall. While incident electrons of some other angle are in nonchanneling conditions, more backscattering electrons will be observed due to higher atomic packing density along incident direction. The secondary electron production coefficient, δ, for the beam-crystal angle condition will also result in a different, higher value of δ for strong interaction. This variation of production coefficient for BSE and SE due to difference in beam-crystal angle relation gives rise to simple mechanism of electron channeling contrast.

This simple mechanism can be made more rigorous by the use of the Bloch wave model in which the channeling effect is considered as a diffraction of the electron wave by the lattice. The incident electron flux can be mathematically represented as a number of standing plane waves, known as Bloch waves, each of which has the periodicity of the lattice and with its wave front parallel to the surface normal. The type I Bloch wave which has nodes at the atomic position will interact weakly with the lattice because of their distance from it, and as a consequence, is not strongly backscattered. The type II Bloch wave has its maximum intensity on the atomic position and is, therefore, strongly backscattered. For interaction with a given set of lattice planes, the proportion of the type I and type II waves differs as a function of the beam-crystal orientation. Since the incident current is constant, the sum of the intensities in the two Bloch waves is constant. But the ratio of these intensities can vary and thus, the backscattering will change. When Bragg's condition for a lattice spacing of d is satisfied (i.e., $2d\sin\theta_\beta = n\lambda$, where λ is the electron wavelength, θ_β is Bragg angle), the two waves are of equal intensity. If incident angle $\theta < \theta_\beta$, the type II wave dominates, and the electrons tend to interact close to the surface which produces larger value of η and δ. For $\theta > \theta_\beta$, the type I wave dominates and more electron channels into crystal and results in lower value of η and δ. As a beam is scanned over a flat crystal, the θ angle changes, and thus, the backscattering signal will vary. At $\theta = \theta_\beta$, a sharp intensity change occurs. For $\theta = 2\theta_\beta$, $3\theta_\beta$, etc., a sharp transition again results.

The electron channeling pattern consists of contributions from many crystal planes, since a real crystal contains a periodic atom arrangement in three dimensions. Thus, each point in the image actually consists of intensity contributions from many different planes, each of which has an intensity vs θ curve. Since significant channeling effects are only observed near Bragg conditions and sharp transitions are obtained, the effects of particular lattice reflections are distinct in the pattern. The bands are observed in regions where $\theta < \theta_\beta$ and the fine lines represent the sharp change in contrast at the Bragg angle for higher order planes. The bands have a width of $2\theta_\beta$, the width is inversely proportional to the lattice plane spacing d and the accelerating voltage. Also different magnification will have different band widths. The projection of the ECP is gnomonic. The angle between bands will be the angle between the corresponding sets of lattice planes.

The quality of the ECP is strongly dependent on the perfection of the crystal. ECP deformation is directly connected with the curvature of crystallographic planes. Therefore, the dislocation can be found from the ECP deformation.

(b) Cathodoluminescence - The dislocation also can be observed in SEM by cathodoluminescence [29]. The decay of the electron-hole pair can be modified by the presence of impurity atoms or physical crystal defects, such as dislocations, leading to shifts in the energy and intensity of the radiation, as well as the time constant of the decay.

(5) X-ray diffraction topography - Many workers have observed individual dislocations by x-ray diffraction, using different techniques [30]. "Section topographs" and "projection topographs" were found more convenient for general survey work. The principle of section topographs is very simple [31]. X-rays diverging from a small source strike a slab of the crystal. The crystal is oriented so that one sheet of characteristic x-ray in the incident beam can be Bragg reflected by a lattice plane which makes a high angle with the face of the slab illuminated by x-rays. Thus, the Bragg reflected rays are transmitted through the crystal and are received on photographic film. If the crystal is not perfect, the film would not show an approximately rectangular patch of uniform blackening.

For "projection topographs", the x-ray beam from a relatively distant x-ray tube passes through the specimen crystal after appropriate horizontal and vertical limitation at the slit [32, 33]. The crystal is set so that Bragg reflection occurs from a lattice plane making a high angle with the face of the crystal slab. A fixed screen intercepts the directly transmitted beam, but allows the Bragg-reflected beam to reach the film. Crystal and film are both mounted on an accurate linear traversing mechanism. During the exposure, they move back and forth together. The two-dimensional pattern appearing on the film is a projection of the crystal slab and its imperfection content.

(6) Birefringence - Even though it is difficult to use birefringence to reveal individual dislocations [34], it has an advantage of not altering the sample and being applicable to continuous observation. Especially, it can provide a dislocation movement information.

The first observation of artificial birefringence caused by plastic deformation of a crystal was in 1815 by Brewster. The nature of the deformation was further investigated by Brilliantow and Obreimow [35, 36]. In 1949, Nye [37] concluded that the plastic deformation which caused the birefringence is "pencil glide." Kear and Pratt [38] and Mendelson [39] have reported the photoelastic pattern in ionic crystals is due to the stress caused by dislocations.

In three-point bending testing of sodium chloride single crystal, the etch pits of dislocation indicated that the plastic deformation is due to the dislocation slip mechanism [37-39]. Before the dislocation theory was established, the slip concept of plastic deformation was defined as the parallel movement of two adjacent crystal regions relative to each other across some plane. The slip always occurs along a particular plane which is called a slip plane. The combination of a plane and a direction lying in this plane along which slip occurs is a slip system. In fact, this parallel movement is caused by dislocation movement. In dislocation concept of slip, slip vector (Burgers vector) and glide plane were used. The glide plane was defined by the dislocation line and the slip vector. When an external shear stress, τ, is applied to a crystal containing dislocations, it produced a force

at right angle to the dislocation line that causes the dislocation to move. This force, F, on a unit dislocation was calculated to be $F = \tau b$, where b is the Burgers vector. In sodium chloride single crystals at room temperature, the slip planes are {110} [40, 41]. The Burgers vectors are <110>.

In crystals, the Frank-Read source [42, 43] emits a series of dislocations. These emitted dislocations frequently pile up on slip planes at barriers such as grain boundaries, second phase, impurities or sessible dislocations [44]. Therefore, there is a high dislocation density in the slip direction of a slip plane. Birefringence of plastic deformation is based on this high dislocation density. In other words, emitted dislocations, which piled up in slip direction and formed a high dislocation density, caused the birefringence.

When one of these dislocations moves out of the crystal, a step of plastic deformation which is equal to Burgers vector, b, can be formed. It is called a slip line. This slip line is the trace of the slip plane at the surface where a slip step appears. A slip band is a combination of these traces of parallel slip planes. Except the traces above, another trace of the slip plane which produces birefringence is also called slip line. The latter is emphasized in this study.

Birefringence caused by plastic deformation in crystals is more complicated than the birefringence caused by elastic deformation in polymers. Even though many studies for the former have been done for a long time [45, 46], still more work is needed to understand some of

the questions, in comparison with the latter which now is well understood.

Three of the six methods of dislocation observation which we discussed above are very useful for the study of micromechanisms of fracture. They are etching, TEM and birefringence.

Photoelasticity

Many polymer materials which are optical isotropic when free of stress become optical anisotropic and display birefringence when they are stressed. If the behavior is elastic, the birefringence persists while loads on the material are maintained, but disappears when the loads are removed. This phenomenon, known as temporary double refraction, was first observed by Brewster in 1816. Obviously, it is caused by the stresses in the elastic body.

For any point in an elastic body, a stress ellipsoid equation can be written as [47]:

$$\frac{T_{nx}^2}{\sigma_1^2} + \frac{T_{ny}^2}{\sigma_2^2} + \frac{T_{nz}^2}{\sigma_3^2} = 1 \qquad (2)$$

where

T_{nx}, T_{ny}, T_{nz} = Cartesian components of the resultant stress

and

σ_1, σ_2, σ_3 = principal normal stresses.

The optical anisotropy which develops in this elastic stress field can also be represented by an index ellipsoid. The changes in the indices of refraction are linearly proportional to the stresses. The following equation established by Maxwell [48] in 1853 can be used to show the stress-index relationship:

$$(\eta_1-\eta_o) = C_1\sigma_1 + C_2(\sigma_2 + \sigma_3)$$

$$(\eta_2-\eta_o) = C_1\sigma_2 + C_2(\sigma_3 + \sigma_1)$$

$$(\eta_3-\eta_o) = C_1\sigma_3 + C_2(\sigma_1 + \sigma_2) \qquad (3)$$

where

η_o = index of refraction of material in unstressed state,

η_1, η_2, η_3 = indices of refraction of material in stressed state associated with principal stress directions (principal indices of refraction) and

C_1, C_2 = constants known as stress-optic coefficients.

The equation above can be rewritten as

$$(\eta_2-\eta_1) = C(\sigma_1-\sigma_2)$$

$$(\eta_3-\eta_2) = C(\sigma_2-\sigma_3)$$

$$(\eta_1-\eta_3) = C(\sigma_3-\sigma_1) \qquad (4)$$

where C is the relative stress-optic coefficient (C_2-C_1). Equation (4) indicates the relationship between stresses and indices of refraction. It is a basis of the birefringence. When a stressed model is placed in a polariscope, the birefringence can be seen.

The simplest polariscope is the dark field plane polariscope. This plane polariscope has a polarizer and an analyzer. The axis of the polarizer is perpendicular to the axis of analyzer. The stressed model is placed between the polarizer and the analyzer. It is so placed that its stress direction, σ_1, has an angle α with the axis of the polarizer. In this dark field plane polariscope, the plane-polarized light beam emerging from the polarizer can be expressed as

$$E_{py} = K \cos wt \quad . \tag{5}$$

This light vector E_{py} is resolved into two components, E_1 and E_2, with vibration parallel to the two principal stresses, σ_1 and σ_2, when it reaches the stressed model:

$$E_1 = K \cos\alpha \cos wt$$

$$E_2 = K \sin\alpha \cos wt \quad . \tag{6}$$

Since E_1 and E_2 propagate through the stressed model with different velocities, they develop phase shifts Δ_1 and Δ_2 with respect to a wave in air. The waves, as the light leaves the model, can be expressed as

$$E_1' = K \cos\alpha \cos(wt - \Delta_1) \tag{7}$$

$$E_2' = K \sin\alpha \cos(wt - \Delta_2) \quad . \tag{8}$$

The Δ_1 and Δ_2 are computed simply as

$$\Delta_1 = \frac{2\pi h}{\lambda} (\eta_1 - 1) \tag{9}$$

$$\Delta_2 = \frac{2\pi h}{\lambda} (\eta_2 - 1) \tag{10}$$

where

h = thickness of the model and

λ = wave length of the light.

When the E_1' and E_2' enter the analyzer, they are resolved into horizontal components E_1'' and E_2''. Then, the E_1'' and E_2'' are combined to produce an emerging light vector E_{ax}, which is given by

$$E_{ax} = E_2'' - E_1'' = E_2' \cos\alpha - E_1' \sin\alpha$$

$$= K \sin 2\alpha \sin \frac{\Delta_2 - \Delta_1}{2} \sin (wt - \frac{\Delta_2 + \Delta_1}{2}) \quad . \tag{11}$$

The intensity of light is then

$$I = K \sin^2 2\alpha \sin^2 \frac{\Delta}{2} \tag{12}$$

where

$$\Delta = \Delta_2 - \Delta_1 = \frac{2\pi h}{\lambda} (\eta_2 - \eta_1) \quad . \tag{13}$$

Substituting Eq. (4) for Eq. (13):

$$\Delta = \frac{2\pi h}{\lambda} C(\sigma_1 - \sigma_2) \quad , \tag{14}$$

and Eq. (14) into Eq. (12):

$$I = K \sin^2 2\alpha \sin^2 \frac{\pi h c}{\lambda} (\sigma_1 - \sigma_2) \quad . \tag{15}$$

Equation (15) is the basic equation for birefringence. It explains the photoelasticity in stressed elastic body.

Fracture Mechanics

In 1921, Griffith [49] established a basic equation in fracture mechanics. He stated that crack propagation can occur if the energy released by the crack growth is enough to provide all the energy of crack growth.

The elastic strain energy per unit of plate thickness is equal to

$$U_E = - \frac{\pi C^2 \sigma^2}{E} \tag{16}$$

where

σ = tensile stress acting normal to the crack,

C = half crack length and

E = Young's modulus.

The surface energy of the crack is

$$U_s = 4C\,\gamma_s \tag{17}$$

where γ_s is the surface energy per unit area. According to Griffith's criterion above,

$$\frac{d(\Delta U)}{dC} = \frac{d(4C\gamma_s - \frac{\pi C^2 \sigma^2}{E})}{dC} = 0$$

$$\sigma_f = \left(\frac{2E\gamma_s}{\pi C}\right)^{1/2} \tag{18}$$

where σ_f is the fracture stress. The equations above developed by Griffith were only for brittle materials. In semibrittle and ductile materials, plastic deformation occurs at the crack tip. Therefore, Griffith's equation for the fracture stress does not apply for those materials. Plastic deformation at the tip of the crack will blunt the tip of the crack, thus the fracture stress can be increased. Orowan [50] modified Griffith's equation (18) by adding γ_p to γ_s:

$$\sigma_f \doteq \left[\frac{E(\gamma_p + \gamma_s)}{C}\right]^{1/2} \tag{19}$$

where γ_p is plastic energy required to extend the crack. The surface energy, γ_s, is much smaller compared with the plastic energy, γ_p. Irwin made a fundamental contribution to fracture mechanics. He suggested that fracture occurs at a fracture stress corresponding to a critical value of the crack-extension force, ξ:

$$\sigma_f = \left(\frac{E\xi}{\pi C}\right)^{1/2} . \tag{20}$$

ξ may also be considered the "strain-energy release rate".

When the problem is extended from elastic to elastic-plastic and plastic, the difficulties in studying fracture increase. Linear elastic mechanics have well-described elastic fracture. The measurement of fracture toughness for brittle materials is well-founded. The situation in the elastic-plastic fracture is not simple. Because of the mathematical difficulties in any elastic-plastic analysis, a satisfactory treatment for evaluating nonlinear elastic fracture toughness parameters is not currently available [51]. However, many attempts have been made to treat the plastic-elastic problem by extending the concepts of linear elastic fracture mechanics. Some of these attempts are crack opening displacement [52, 53], R curve [54] and J integral [55].

There are two approaches to treat elastic-plastic problems [56]. One is to establish nonlinear fracture toughness parameters by using the nonlinear stress-strain relation near the crack tip. As mentioned above, there are difficulties in the mathematical analysis necessary to

establish a modified equivalent elastic problem for a nonelastic one. The other is to analyze the total energy balance associated with crack extension. This energy balance approach is not restricted to the usual limitation of the elastic theories. Therefore, it is very effective in practical analysis.

An empirical method for evaluating the fracture parameters, which include the work of fracture, the elastic energy release, the plastic energy dissipation and the crack propagation resistance, is proposed by using loading (p) versus load point displacement (δ) diagram [56]. Usually, a specimen with sharp and deep notches was tested in three-point bending at slow test speed to obtain a stable p-δ diagram for measuring the fracture toughness parameters [57].

EXPERIMENTAL PROCEDURE

Determination of the Burgers Vector

In order to understand dislocation movement, it is necessary to determine the Burgers vector using TEM.

The sodium chloride single crystals used for TEM observations cannot be prepared by electropolishing or mechanical methods because they are brittle and soluble. To make a suitable sample for TEM, the single crystal was cut with a string saw into 1 x 1 x 0.2 cm plates, using water as the solvent. The plates were thinned to about 200 μm by dissolving with water on a nylon lap, and allowed to rest in 50% ethanol - 50% water until they were 50 μm thick. Then, they were cleaved to small pieces which could be mounted on double layer grids. A droplet of water was placed on the center of the specimen with a microsyringe. It was then absorbed with a lint-free tissue. This procedure was repeated until first order and second order interference colors, which were near the central hole, were seen with a reflecting microscope at 600X. The thickness of the sample in this condition is thin enough for electron transmission [58].

The samples were coated with carbon. For the observation of dislocations in sodium chloride, carbon coating is much better than gold. Because sodium chloride is not an electrical conductive material, the coating layer should be thick enough to produce good conductivity. But it is necessary to avoid diffraction ring patterns from the coating materials.

The coated samples were mounted on the double tilting stage of a JEOL 100 CX scanning transmission electron microscope. An 80 KV accelerating voltage was selected. Convergent beam microdiffraction was used to obtain very clear Kikuchi lines [59]. From the Kikuchi patterns of sodium chloride, the two-beam conditions were located. Because sample damage by the electron beam is always a problem with ionic materials, quick operation was necessary. The following reciprocal vectors, g, were selected: $g = (0\bar{2}0)$, $g = (200)$, $g = (220)$ and $g = (020)$. Bright field images of dislocations under the two-beam kinematic conditions above were observed on the screen [60]. Table 2 lists the visible or invisible nature of dislocation images on the screen at each g. Some possible Burgers vectors are also listed in this table. It shows that in sodium chloride at room temperature, the Burgers vectors are <101> type.

Sample Preparation for One Active Slip System

In this study, two types of sodium chloride samples were needed. One type was for studying the relationship between birefringence and dislocation movement. In this type, sample preparation to provide one active slip system was required. Another type was for measuring the fracture toughness parameters. In this type, sample preparation for fully stable fracture was required. The first type is discussed first.

Optical grade sodium chloride was obtained from the Harshaw Chemical Company in the form of bulk ingots. Semi-quantitative

Table 2. Values of g·b for the reflections and the $\alpha/2$ <110> Burgers vectors in f.c.c

Reflection	Possible Burgers vector						Disloc. line image
	$\pm[110]$	$\pm[1\bar{1}0]$	$\pm[101]$	$\pm[10\bar{1}]$	$\pm[011]$	$\pm[01\bar{1}]$	A
$0\bar{2}0$	± 1	± 1	0	0	± 1	± 1	invisible
200	± 1	± 1	± 1	± 1	0	0	visible
220	± 2	0	± 1	± 1	± 1	± 1	visible
020	± 1	± 1	0	0	± 1	± 1	invisible

spectrographic analysis showed the bulk ingot contained very faint traces of silicon and copper and faint traces of aluminum and magnesium. Test samples were taken from a large ingot which had size D 210 x 65 mm to avoid the variation of impurities and quality that might occur from ingot to ingot. Small external forces can damage the sodium chloride single crystals easily, so very careful handling was necessary. In order to cut this large ingot into test pieces of the required size (approximately 8 x 14 x 50 mm) without damage, a string saw was used (Figure 1). Distilled water was used as the solvent on the string. After cutting, samples were annealed at 740°C for 6 hrs. To observe dislocations, some samples need to be etched. Because only fresh cleavage surface can be etched to show the dislocations, the samples which need to be etched were cleaved by a small sharp knife. When annealing was conducted, the crucibles containing these samples were sealed with a cover to avoid thermal etching during the annealing.

A solution of 10 g/ℓ $HgCl_2$ in ethanol was used to etch dislocations. The tested samples were immersed in the solution for 20 seconds, and then were washed with acetone. After drying, they were observed with a polarizing microscope.

Because the stress state and dislocation movement depend on the sample size, proper selection of sample size is important. At room temperature in sodium chloride single crystal, there are three types of slip planes [40]. They are type (110) slip plane which includes $(1\bar{1}0)$ slip plane (Figure 2), type (101) slip plane which includes $(10\bar{1})$ slip plane (Figure 3) and type (011) slip plane which includes $(01\bar{1})$

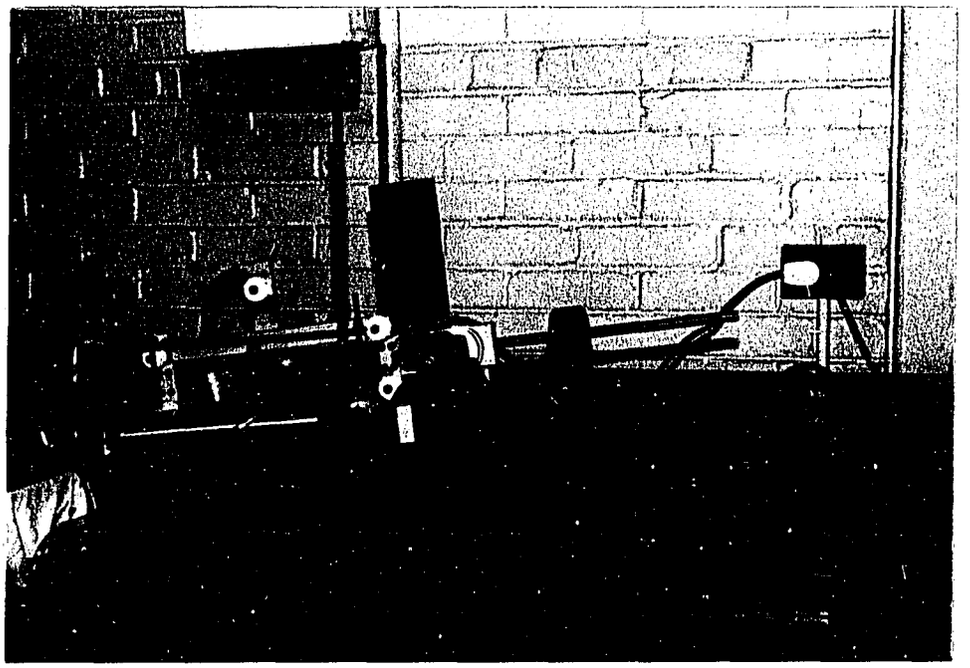

Figure 1. String saw for cutting sodium chloride ingot

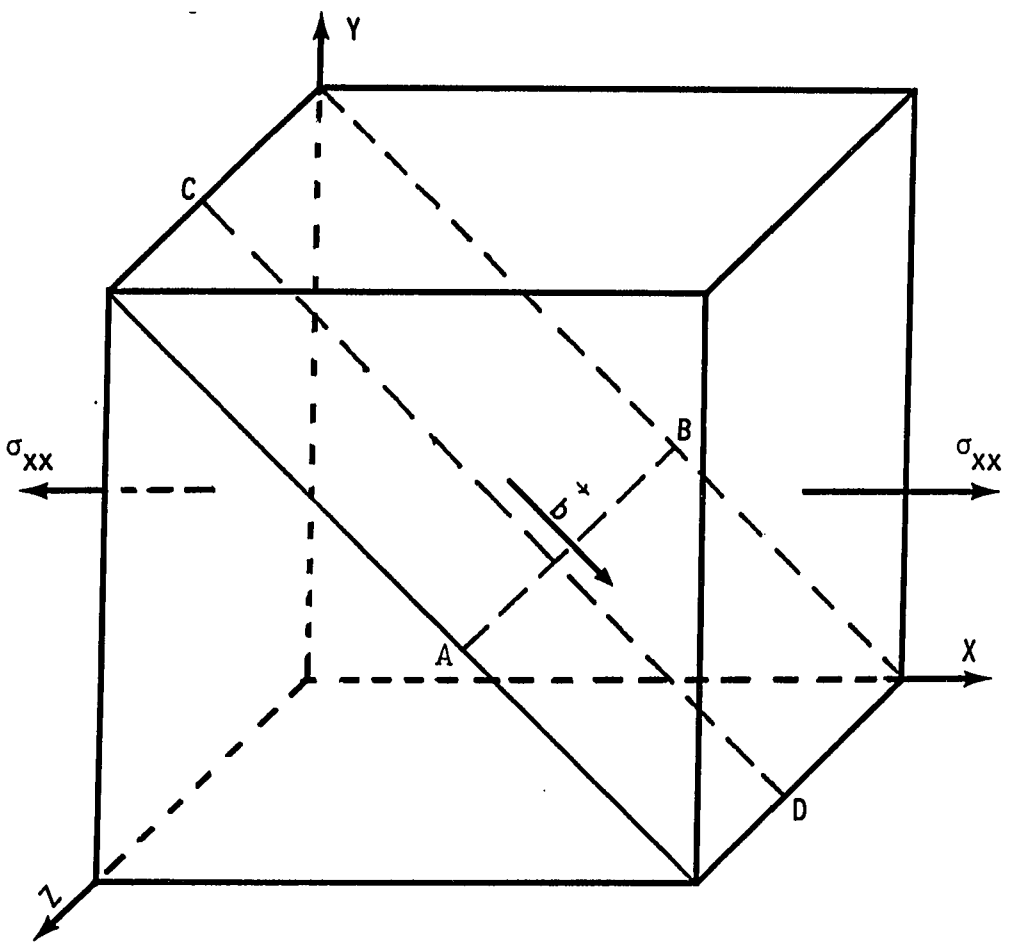

Figure 2. (110) slip plane in sodium chloride

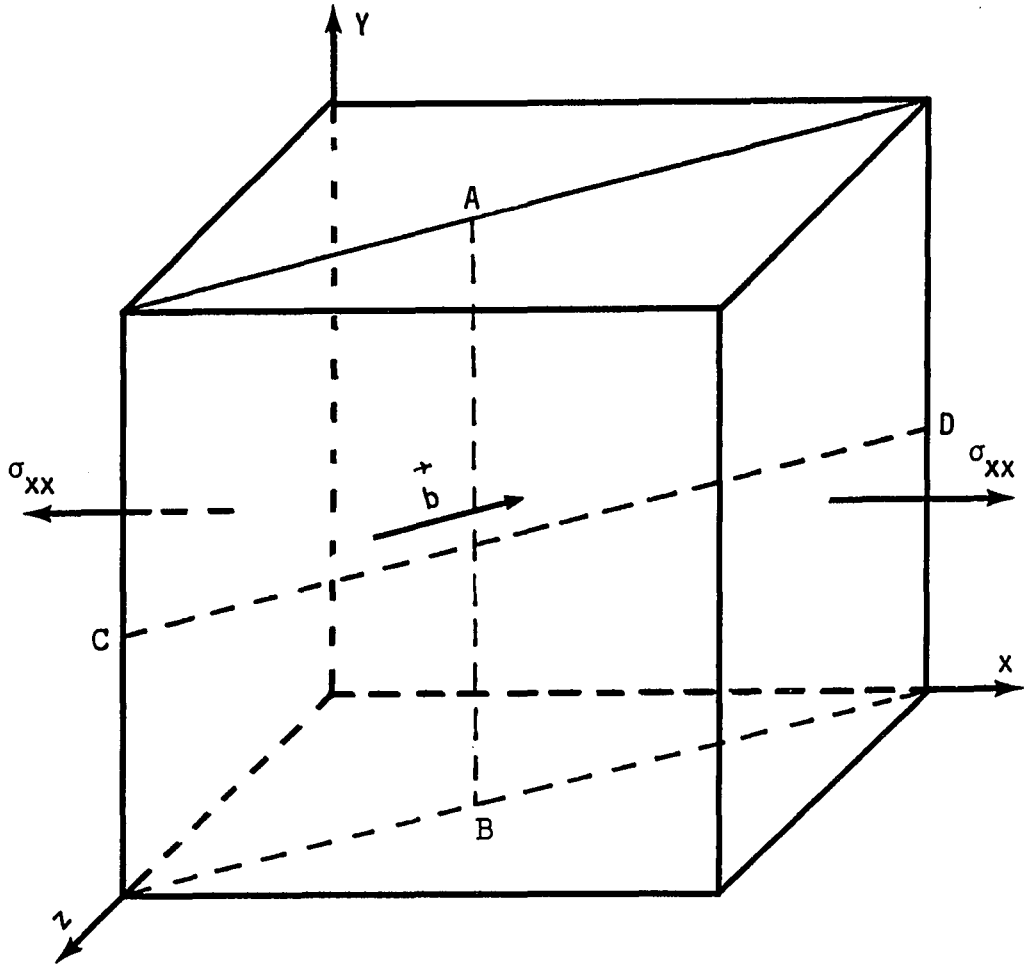

Figure 3. (101) slip plane in sodium chloride

slip plane (Figure 4). At room temperature, the Burgers vectors were found to be $\frac{1}{2}$ <110> by electron microscopy. The simplified possible dislocation lines and the $\frac{1}{2}$ <110> Burgers vectors are also listed in the figures above. The $\frac{1}{2}$ <100> Burgers vectors are not active at room temperature.

To study the relationship between photoelasticity and dislocation movement in sodium chloride single crystals, only one active (110) slip plane is desired if the light path in a polariscope is in the Z direction (Figure 2). This is because, with the one active (110) slip plane condition, the front surface of Figure 2 has only the trace of edge dislocations. Any more active slip planes can lead to the trace of a screw dislocation on the front surface. This would make it difficult to analyze the relationship between birefringence and the dislocation slip line.

When comparing Figures 2 and 3, if only σ_{xx} normal stress is given, in a plane stress condition this force can generate both (110) slip plane and (101) slip plane. Figures 5 and 6 show the results. Figure 5 is the dislocation slip lines on the top surface (010) of Figures 2 and 3. The 45° dislocation slip lines are the edge dislocation pile ups of (101) plane. The perpendicular slip lines are the screw dislocation pile ups of (110) plane. Figure 6 is the dislocation slip lines on the front surface (001) of Figures 2 and 3. The 45° dislocation slip lines are the edge dislocation pile ups of (110) plane. The perpendicular slip lines are the screw dislocation pile ups of (010) plane.

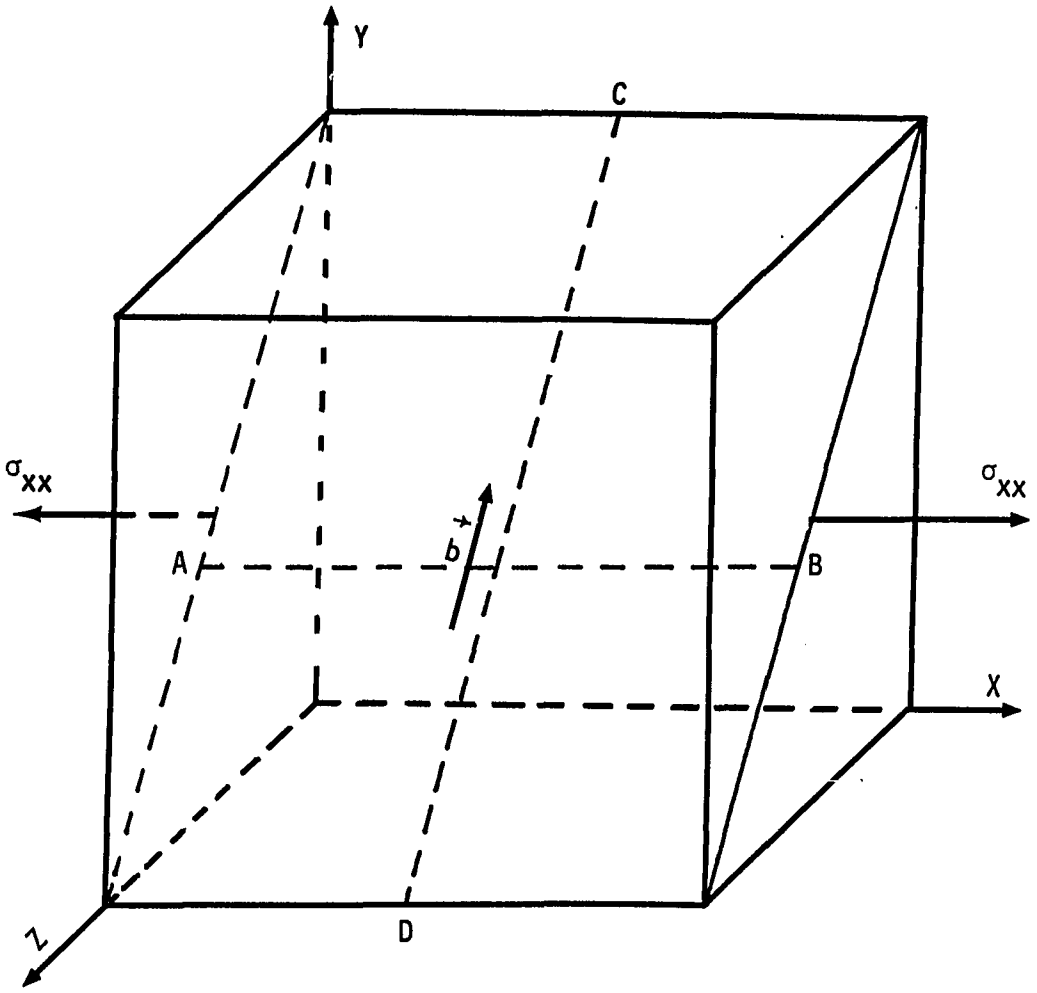

Figure 4. (011) slip plane in sodium chloride

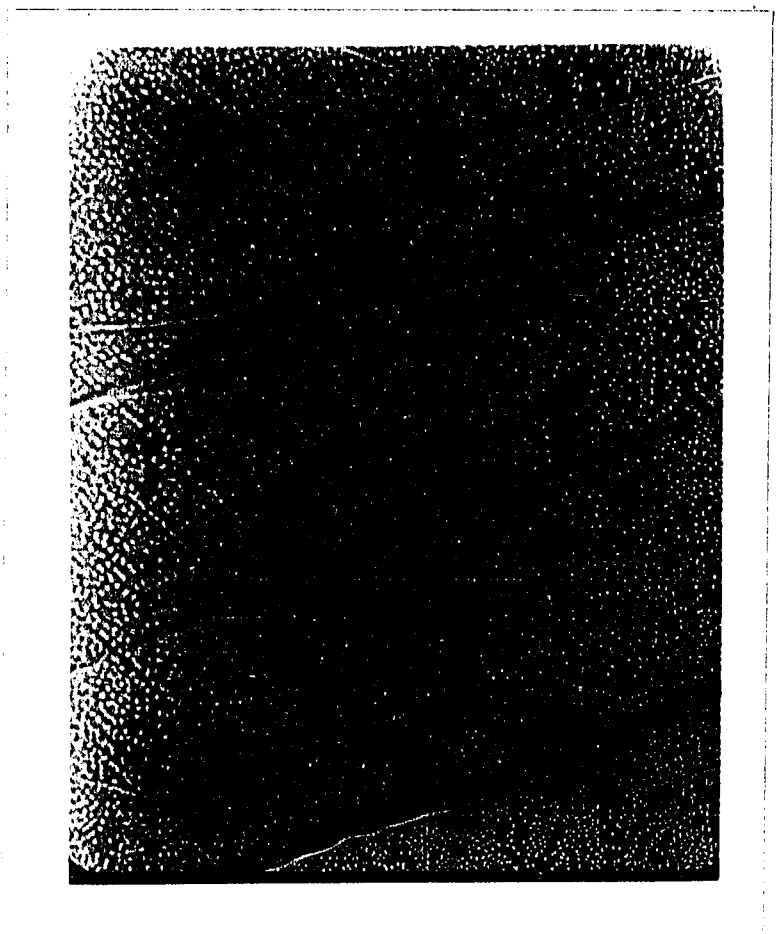

Figure 5. Dislocation slip lines on the top surface (010) of Figures 2 and 3. X200

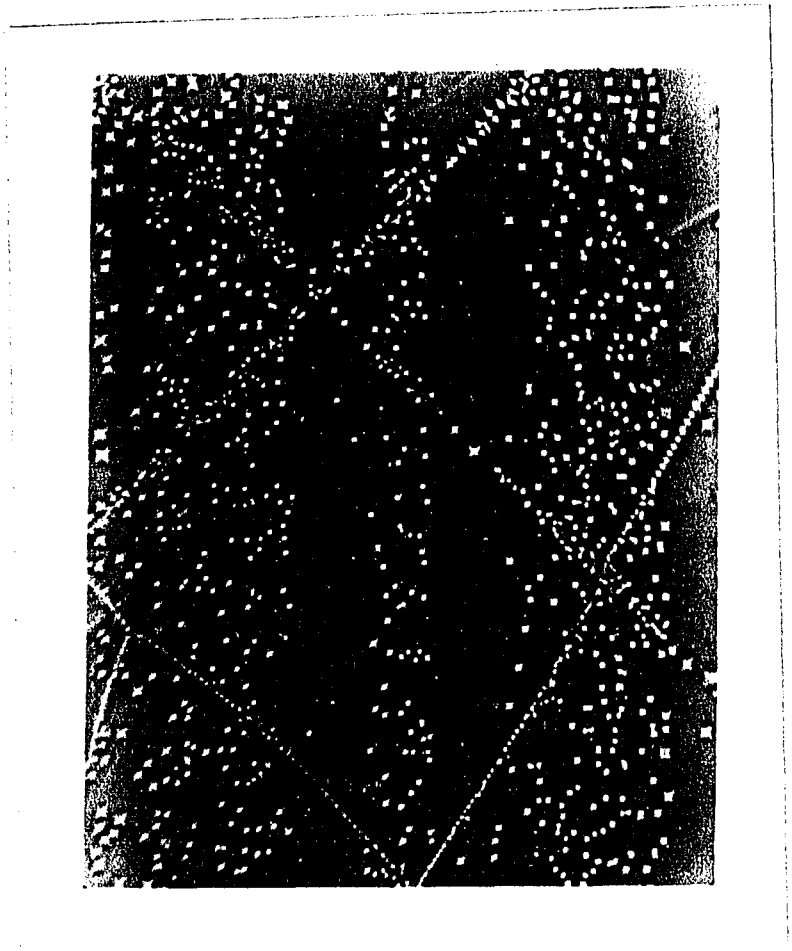

Figure 6. Dislocation slip lines on the front surface (001) of Figures 2 and 3. X300

In order to generate only one active (110) slip plane, a σ_{zz} normal stress is required. A thick sample can produce a plane strain condition to satisfy this requirement. The introduced σ_{zz}, under a plane strain condition, does not change anything on the dislocation movement of the (110) slip plane of Figure 2. But, it can stop the dislocation movement on the (101) slip plane of Figure 3. Let us consider the edge dislocation line $\overline{AB}$ with Burgers vector b in Figure 3. If both the normal stresses σ_{xx} and σ_{zz} act on the sample, the force on a unit dislocation of $\overline{AB}$ can be written as

$$F = S \times G = \begin{vmatrix} i & j & k \\ S_x & S_y & S_z \\ G_x & G_y & G_z \end{vmatrix} = G_z i - G_x K \tag{21}$$

$$G = \begin{pmatrix} \sigma_{xx} & \sigma_{xy} & \sigma_{xz} \\ \sigma_{yx} & \sigma_{yy} & \sigma_{yz} \\ \sigma_{zx} & \sigma_{zy} & \sigma_{zz} \end{pmatrix} \cdot \begin{pmatrix} b_x \\ b_y \\ b_z \end{pmatrix} = \begin{pmatrix} \frac{b\,\sigma_{xx}}{\sqrt{2}} \\ 0 \\ \frac{b\,\sigma_{zz}}{\sqrt{2}} \end{pmatrix} \tag{22}$$

Substituting Eq. (22) into Eq. (21) produces:

$$F = \frac{-b\sigma_{zz}}{\sqrt{2}} i - \frac{b\sigma_{xx}}{\sqrt{2}} K$$

$$= \frac{-b}{\sqrt{2}} (\sigma_{zz} i + \sigma_{xx} K) \tag{23}$$

where

F = force on a unit dislocation line of $\overline{AB}$,

i, j, k = unit vectors in the x, y and z directions,

S_x, S_y, S_z = three components of the unit dislocation line of $\overline{AB}$,

b_x, b_y, b_z = three components of the Burgers vector b and

$\sigma_{xx}, \sigma_{xy}, \sigma_{xz}, \sigma_{yx}, \sigma_{yy}, \sigma_{yz}, \sigma_{zx}, \sigma_{zy}, \sigma_{zz}$ = cartesian components of stress.

This force on a unit length of the dislocation line $\overline{AB}$ is illustrated in Figure 7. Obviously, the introduced positive σ_{zz} reduces the shear stress on slip plane (101). Thus, the dislocations in (101) plane cannot move. The experiment showed that a 6 x 8 x 14 mm sample of sodium chloride single crystal in a three- or four-point bending can produce a plane strain condition with $\sigma_{xx} > \sigma_{yy}$ and σ_{zz}. In this condition, only one active (110) slip plane can be seen. Figures 8 and 9 show this result.

Sample Preparation for Fully Stable Fracture

The work of fracture technique was used to measure the work of fracture of sodium chloride single crystals. This technique employs three-point bending of a deeply notched sample. Figure 10 illustrates the load/deflection relationship in the work of fracture measurement for fully stable crack propagation. In this fully stable condition, the energy balance can be written as [61]:

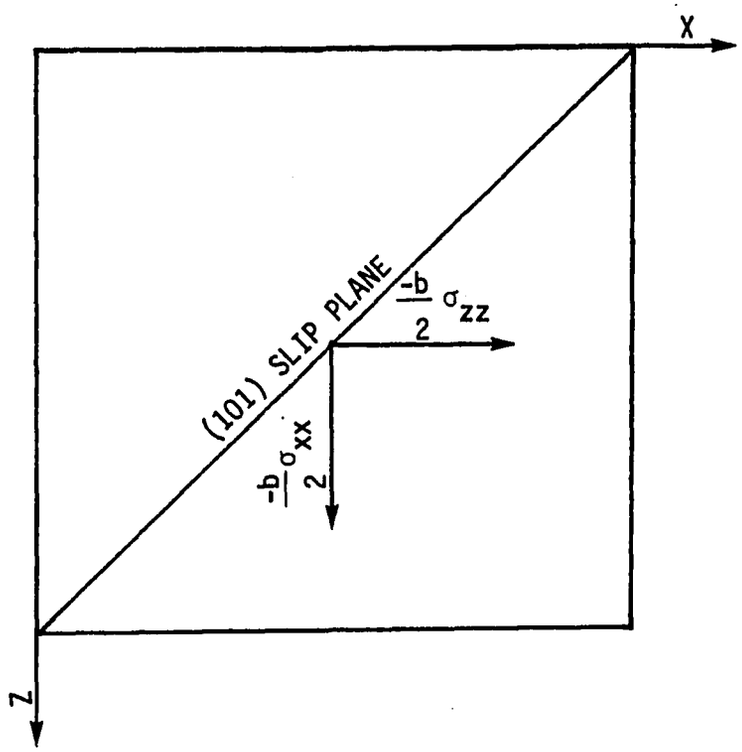

Figure 7. Force on a unit length of the dislocation line $\overline{AB}$ in Figure 3

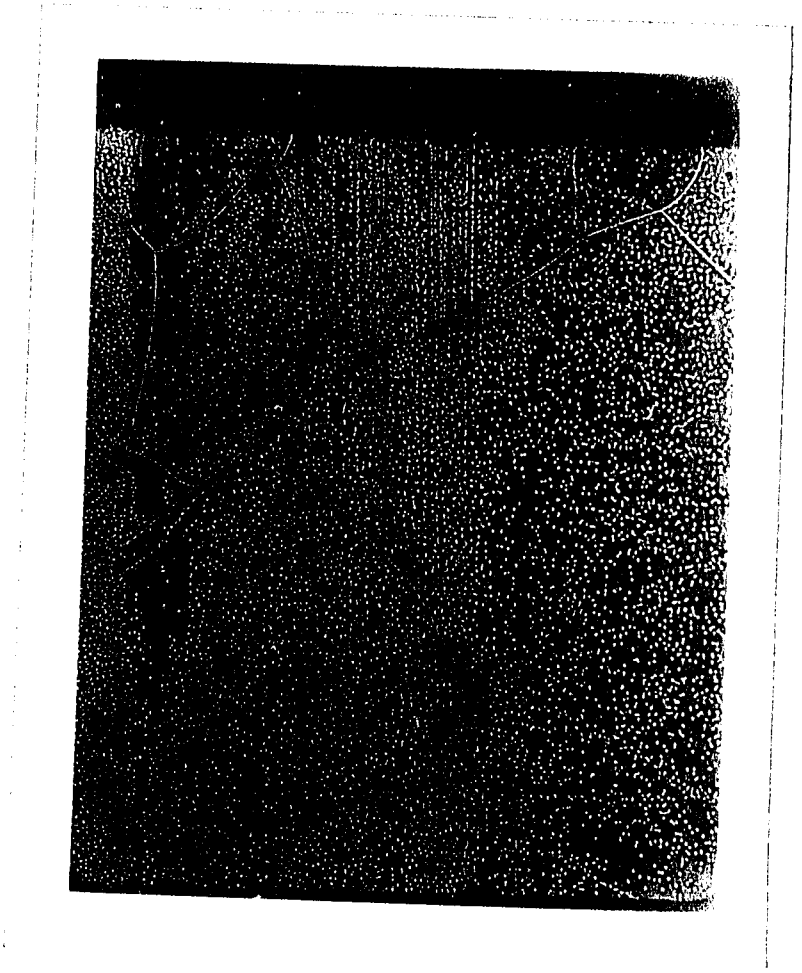

Figure 8. Dislocation slip lines on the top surface (010) of Figure 2. There is no 45° edge dislocation slip on (101) plane. X200

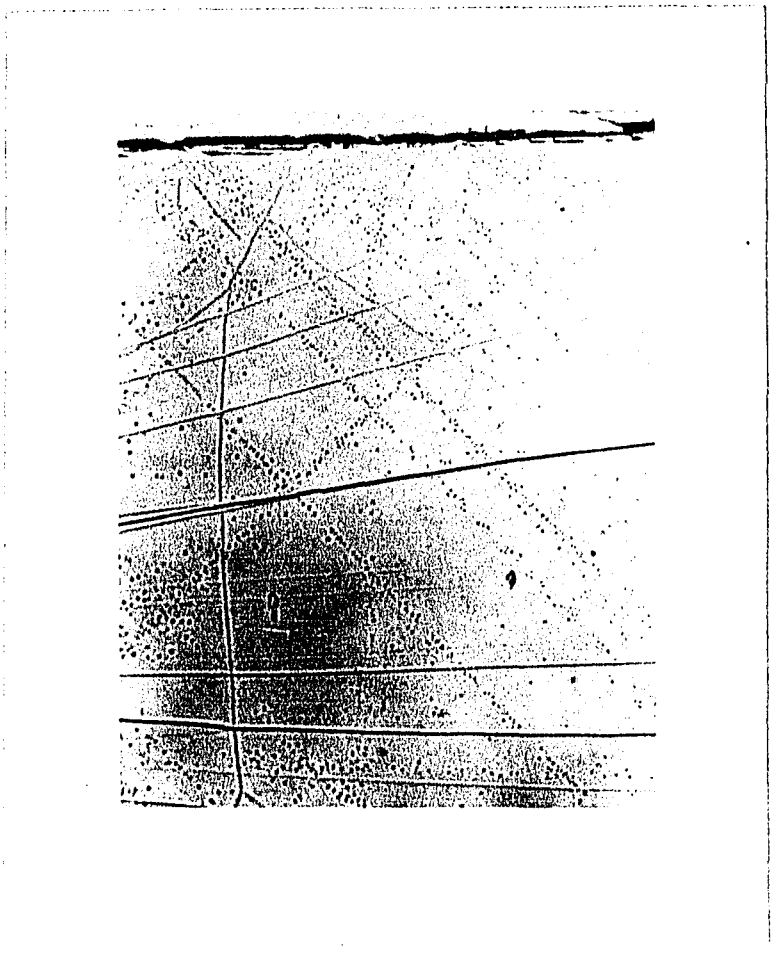

Figure 9. Dislocation slip lines on the front surface (001) of Figure 2. There is no perpendicular screw dislocation slip on (101) plane. X200

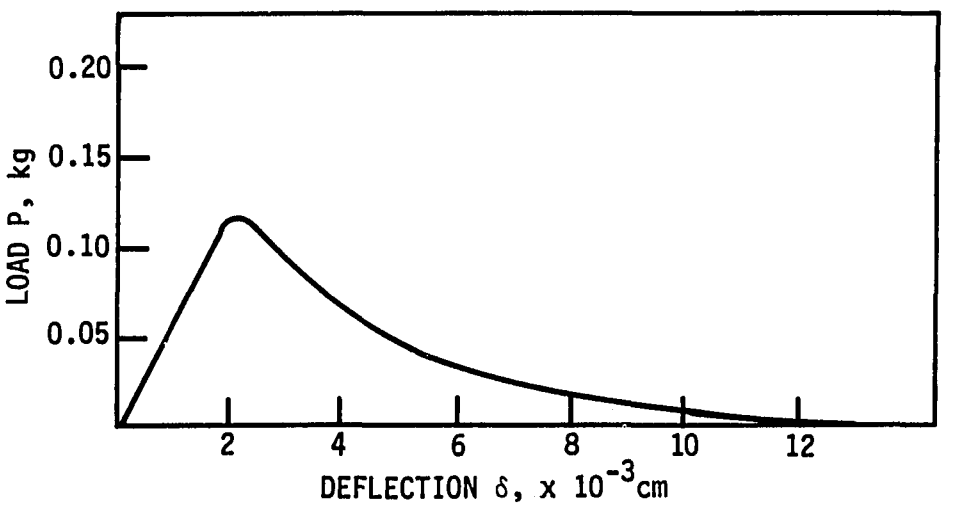

Figure 10. Typical p-δ trace for a stable fracture of sodium chloride single crystal in liquid N_2

$$pd\delta = W_{wof}\, dA + d\phi \qquad (24)$$

where

p = load,

δ = deflection,

A = area of crack surface,

W_{wof} = average energy expended during crack propagation per unit area of crack surface and

ϕ = energy expended in regions remote from the crack.

Good sample size and instrument design in the bending testing were required to limit ϕ to be as near as possible to zero. Figure 11 shows the dimensions of test specimens and the positions of the rollers. First, the contact surface of the rollers and the sample should be smooth. If the contact surface is rough, friction between the rollers and the sample will increase the integral area under load (p) - deflection (δ) curve [62]. Then, the span for three-point bending should be long [63]. Otherwise, serious stress concentration at each roller is possible. This serious stress concentration can lead to plastic deformation near the roller. Therefore, ϕ will not be zero. This can be checked by the birefringent images of tested sodium chloride single crystals. If there is no birefringent image at each loading point, then ϕ can be presumed to be negligible. Then,

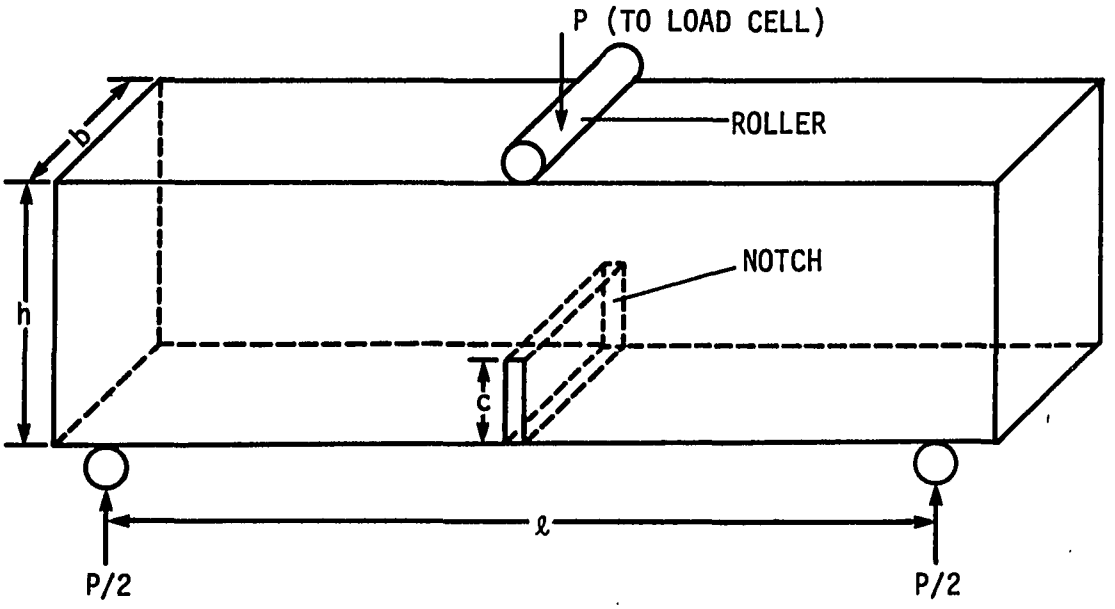

Figure 11. Geometry and dimensions of test specimens

$$W_{wof} = \frac{\int_0^{\delta_t} p d\delta}{2Ac} \tag{25}$$

where Ac = cross-sectional area of the fracture,

δ_t = deflection at the total failure and

W_{wof}, δ and p are defined as in Eq. (24).

Also good sample design, including the selection of the ratio of the notch depth to sample thickness [64], and good test parameters, including the compliance of the testing system [65, 66] and the test speed, are required to satisfy the requirements for fully stable crack propagation. For three-point bending of a sharp notched sample, the total energy of the test system can be expressed as [67]:

$$U_T = U_S + U_M + U_K + W_{wof} \tag{26}$$

where

U_T = total energy of the test system,

U_S = elastic energy in the sample,

U_M = elastic energy in the machine,

U_K = kinetic energy loss and

W_{wof} = fracture work.

The test speed (cross-head speed) used is less than 0.002 cm/min, so the U_K is negligible for this slow test speed [67]. The required condition for a stable fracture can be expressed as

$$-\left[\frac{d(U_S + U_M)}{dc}\right] \leq \frac{d\, W_{wof}}{dc} \quad . \tag{27}$$

An evaluation of the machine and specimen parameters for this stable fracture can be written [67]:

$$\frac{\nu_n h \ell}{C^2}\left\{1 + \frac{1.2\, h^2 E}{\ell^2 G}\right\} + \frac{\nu_n h^2}{C^2} + \frac{\nu_n E b h^4 \lambda}{\ell^2 C^2} \leq W_{wof} \tag{28}$$

where

ν_n = crack initiation energy,

h = height of the sample,

ℓ = length of the sample,

b = thickness of the sample,

C = notch depth,

E = specimen's Young's modulus,

G = specimen's shear modulus,

λ = machine compliance and

W_{wof} = work of fracture.

A hard load cell DM of Instron was used to reduce the elastic stored energy in the test system. The experiment shows that for the same test conditions, the soft load cell CCM of Instron cannot produce an ideal fully stable fracture. The selected sample size was ℓ = 50 mm, b = 7 mm and h = 10 mm. In order to get a stable fracture, the sample was notched with a deep notch of C/h = 0.7. Equation (28) indicates

that the stable condition depends on the test machine characteristics, the notch geometry and depth, and the physical properties of the specimen material. The parameters above for stable fracture can be changed relative to each other to satisfy Eq. (28). Usually, stable propagation of a crack is achieved on a trial and error basis. However, the value of (C/h) is the most important parameter.

Design of Pyrogenic and Cryogenic Systems

The experimental samples were tested at room temperature, at a high temperature (up to 300°C) or at a low temperature (in liquid N_2). Pyrogenic and cryogenic systems were designed for these experiments.

A special small furnace was designed to heat the samples (see Appendix B, Figure 33). Two window holes of D 15 mm were made on the opposite ends of the furnace to observe the birefringence of the sample to be heated. The sample was placed in the center of the furnace. The polariscope arrangement was as follows. The light source was a bulb. The light from the bulb enters the polarizer, and the polarized light from the polarizer passes the first window hole. Then, it reaches the sample at the center of the furnace for the three-point bending testing (the three-point bending was previously discussed). Then, the light passes the second window hole at the opposite end of the furnace and reaches the analyzer. The furnace was designed so that the samples can be changed easily. To do this, a split design was used for easy opening and closing. The thermocouple to control the

temperature was set near the inside furnace wall. The temperature of the furnace was controlled by an Electromax V-Plus general-purpose single-loop controller. A temperature recorder was used to record the temperature at the specimen using a separate thermocouple. The experiment showed that when the tip of the thermocouple of temperature controlling was away from the inside wall of the furnace, the temperature change in the center of the furnace was about $\pm$ 3°C. When it was near the wall of the furnace, the temperature change was smaller than the previous case. If a constant speed of cooling water was maintained to cool the force rod and the sample supporting rod for three-point bending in the furnace, a $\pm$ 0.5°C temperature change in the sample place of this furnace could be obtained. This furnace was also designed so that it took less than 10 minutes to heat the replaced sample to the holding temperature.

For three- or four-point bending testing at room temperature, the small furnace can be removed for convenience.

A simple and very economical method was used to obtain the cryogenic system. The test sample was placed in a beaker of 250 ml in which two rollers supported the sample for the three-point bending test. Liquid N_2 was poured in this beaker to cover the specimen. To reduce the heat conduction from the beaker into the Instron machine, an alumina block was inserted between the beaker and the fixed cross-head of the Instron. The alumina block was designed as a "Λ" shape so that there is a plane contact surface between the beaker and the alumina block and a line contact between the alumina block and the fixed

cross-head of the Instron. The load cell was at the top of an alumina rod of 8 mm diameter. This alumina rod was fixed to the load cell as a force rod. The lower part of this force rod was immersed in the liquid N_2 to conduct the three-point bending. The purpose of using this alumina rod was to reduce the heat conduction by replacing metal with a lower conductivity alumina block. Another advantage of using alumina is its small thermal expansion coefficient. Since alumina has a small thermal conduction coefficient and expansion coefficient, it gives precise test results. This can be explained as follows. In three-point bending of fracture work tests, we calculate the external work by the product of load and displacement. The displacement is the product of force rod speed and time. If there is a thermal expansion or contraction during the test, it means that the force rod speed may change. The result will be different from the constant speed which is intended. Therefore, it is best if no change in thermal expansion occurs during the test.

The cryogenic system described above was isolated by fiberfrax, a ceramic wool insulation. Because there is always a layer of white frost on the outside surface of the beaker due to liquid N_2, it is difficult to use a polariscope to observe the birefringence of the sodium chloride in the center of the beaker.

RESULTS AND DISCUSSION

Birefringence in Sodium Chloride Single Crystals

Birefringence of the edge dislocation slip line

An unannealed sodium chloride single crystal generally has many dislocations with a random distribution. Figure 12 illustrates these random distribution dislocations in addition to the trace of a 45° AB edge dislocation slip line. The 45° edge dislocation slip line, AB, was introduced by an external shear stress. The experiment shows that the dislocations of random distribution do not give any fringe patterns of photoelasticity. Only the AB edge dislocation slip line produced a visible photoelastic fringe pattern. This AB edge dislocation slip line may be long or short. It can be stopped by subgrain boundaries, some impurities, sessile dislocation and so on. Once the external force is big, it may pile up from top surface to the bottom surface. Closer examination of the slip line AB in Figure 12 revealed many small single pile up groups. Figure 13 is an example of a single pile up group.

Figure 12 illustrates only one slip line. If the external load increases, the slip line becomes longer. At the same time, many separate 45° parallel edge dislocation slip lines which are nearby combine together and form a slip band. This is illustrated in Figure 14, which is in one active slip system condition.

In a slip band of Figure 14, each edge dislocation slip line can generate a step on the top surface plane (010) when an edge dislocation

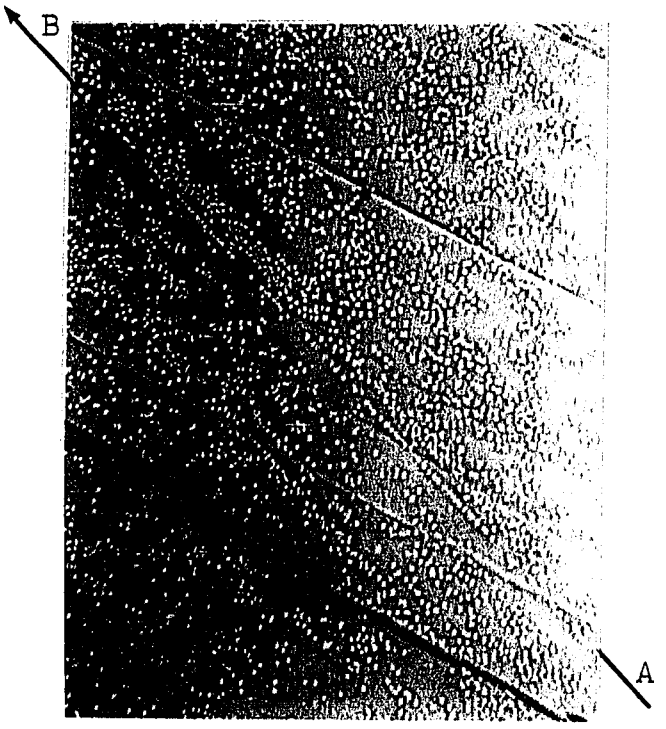

Figure 12. An unannealed sodium chloride single crystal has many random dislocations. Only AB line is a pile up line. X200

Figure 13. A single pile up group from a long pile up line. X280

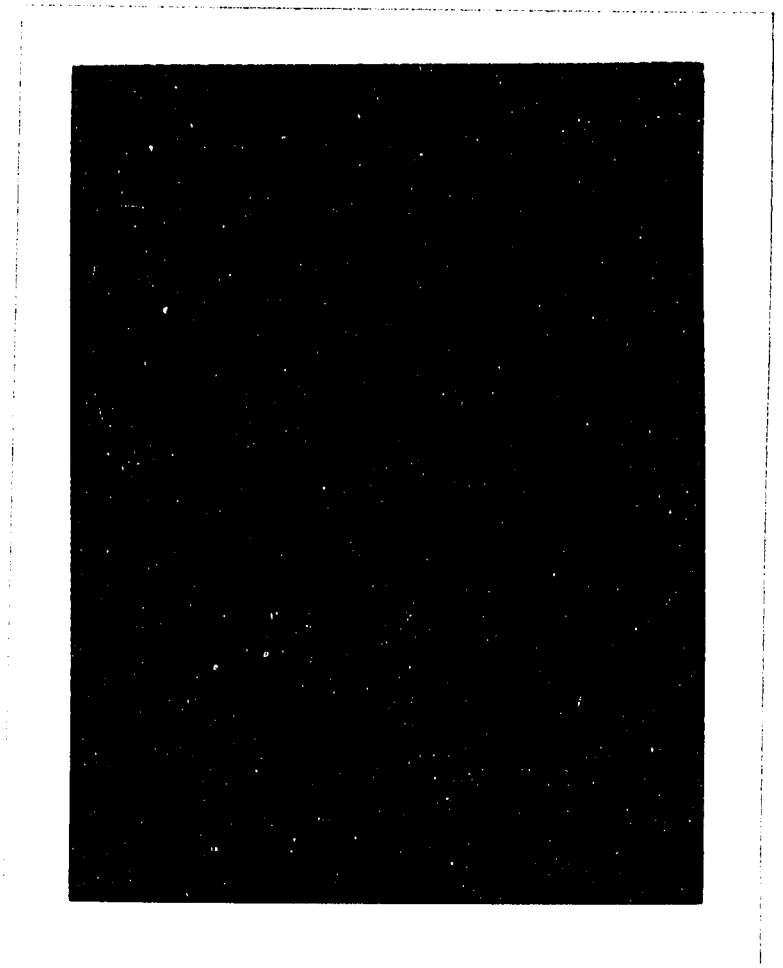

Figure 14. Many parallel dislocation slip lines are combined together and form a wide slip band. X200

in this slip line moved out. The height of these steps is a linear function of the number of dislocations which moved out of crystal. Once the height of these steps of each slip plane is high enough, a step line can be seen with a scanning electron microscope or an optical microscope. Figure 15 illustrates slip step lines which correspond to the slip bands of Figure 14. Obviously, both slip lines and slip step lines are not uniform in distribution.

A dark field polariscope experiment shows that each 45° edge dislocation slip line appears as a bright fringe pattern of photoelasticity when this edge dislocation slip line is 45° from the axis of the polarizer. Figure 16 shows the photoelastic fringe patterns of the 45° edge dislocation slip bands. Each of the photoelastic fringe patterns always corresponds to an edge dislocation slip band. A conclusion can be made from the experiment as follows: an edge dislocation slip line can certainly produce a birefringence image.

Stress field of the edge dislocation pile up

In fact, the experimental conclusion above can be proved by the stress field of the dislocation pile up. For a single edge dislocation, the stress field in rectangular coordinates can be expressed as

$$\sigma_{xx} = - Dy \frac{(3x^2 + y^2)}{(x^2 + y^2)^2}$$

$$\sigma_{yy} = Dy \frac{(x^2 - y^2)}{(x^2 + y^2)^2}$$

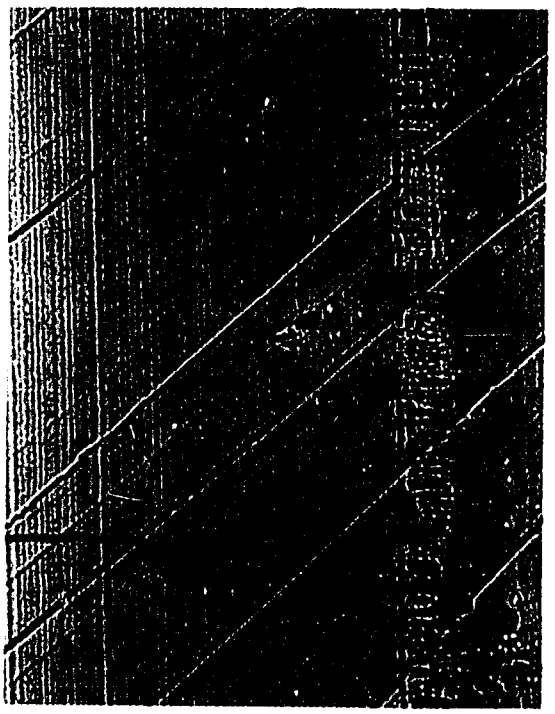

Figure 15. Step lines on the top surface (010) plane. These step lines correspond to the slip bands of Figure 14

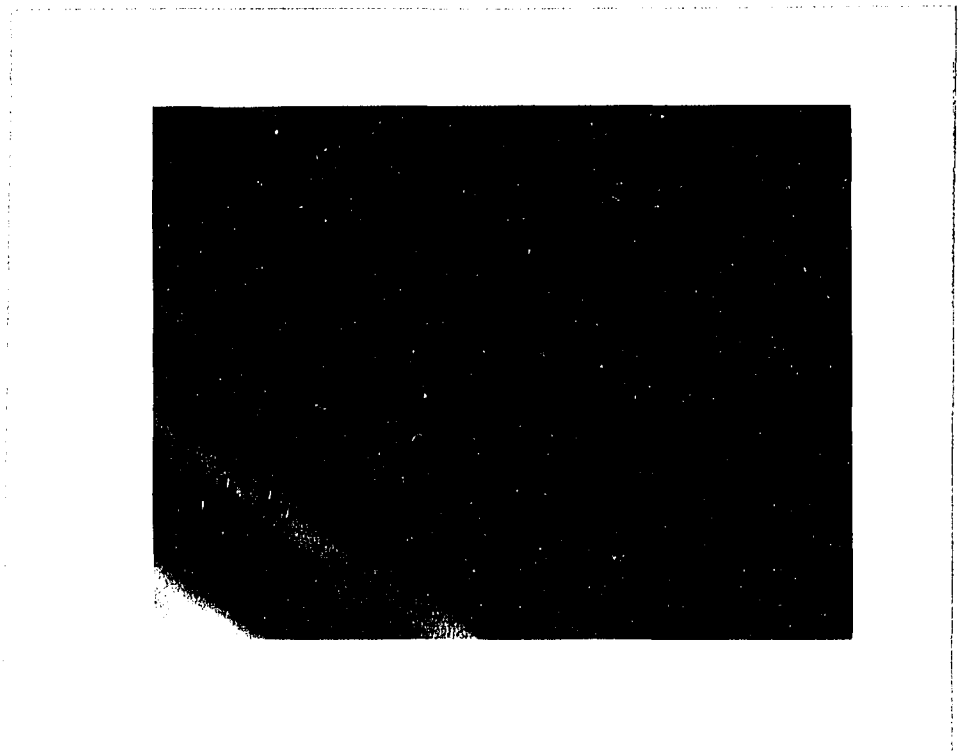

Figure 16. Photoelastic image of the 45° edge dislocation slip bands

$$\sigma_{xy} = \sigma_{yx} = Dx \frac{(x^2 - y^2)}{(x^2 + y^2)^2}$$

$$\sigma_{zz} = \nu(\sigma_{xx} + \sigma_{yy})$$

$$\sigma_{xz} = \sigma_{zx} = \sigma_{yz} = \sigma_{zy} = 0 \qquad (29)$$

where

$D = \frac{Gb}{2\pi (1 - \nu)}$,

ν = Poisson's ratio,

G = shear modulus,

b = Burgers vector (b is in x direction) and

$\sigma_{xx}, \sigma_{yy}, \sigma_{zz}, \sigma_{xy}, \sigma_{xz}, \sigma_{yx}, \sigma_{yz}, \sigma_{zx}, \sigma_{zy}$ = nine stress components of stress at a point.

When there is an edge dislocation pile up on a slip line, many edge dislocations line up in the x direction, i.e., b direction. For this edge dislocation pile up line (slip line), if superimposition of stress fields of each edge dislocation expressed by Eq. (29) is used, at any given point around the slip line, each edge dislocation has the same y value. But, the x values of the dislocations which are located in the positive x direction of this given point are negative. The x values of the dislocations which are located in the negative x direction of this given point are positive. Therefore, according to superimposition of Eq. (29), the σ_{xx} of each dislocation increases with each other

everywhere near the pile up line. Thus, in general, for each dislocation in a pile up line, σ_{xx} can be considered as a principal stress, σ_1. This is especially true for regions $|x| > |y|$. In these regions, σ_{yy} of each dislocation also increases with each other. But for σ_{xy} and σ_{yx}, some cancellation occurs. Therefore, σ_{xy} and σ_{yx} can be ignored. And then, σ_{yy} and σ_{xx} are the principal stresses. Because the pile up direction is the b Burgers vector direction (i.e., x direction), we can make a conclusion that near the pile up line, the principal stresses σ_1 and σ_2 are parallel and perpendicular to the pile up line.

We know that a transparent sodium chloride single crystal is optically isotropic if free of stress. When it is stressed above the yield point, there is dislocation generation and pile up. As we discussed above, due to this pile up, an elastic stress field in which σ_1 and σ_2 are parallel and perpendicular to the slip line exists. Thus, the stressed sodium chloride single crystal becomes optically anisotropic and displays double refraction. This double refraction persists even though the load on the body is removed. This is because the dislocations still exist after the load is removed.

The above conclusion can be proved by the birefringent phenomena in sodium chloride single crystals. Figure 17 illustrates a stressed sodium chloride single crystal model in a plane polariscope. Equation (15) can be rewritten as

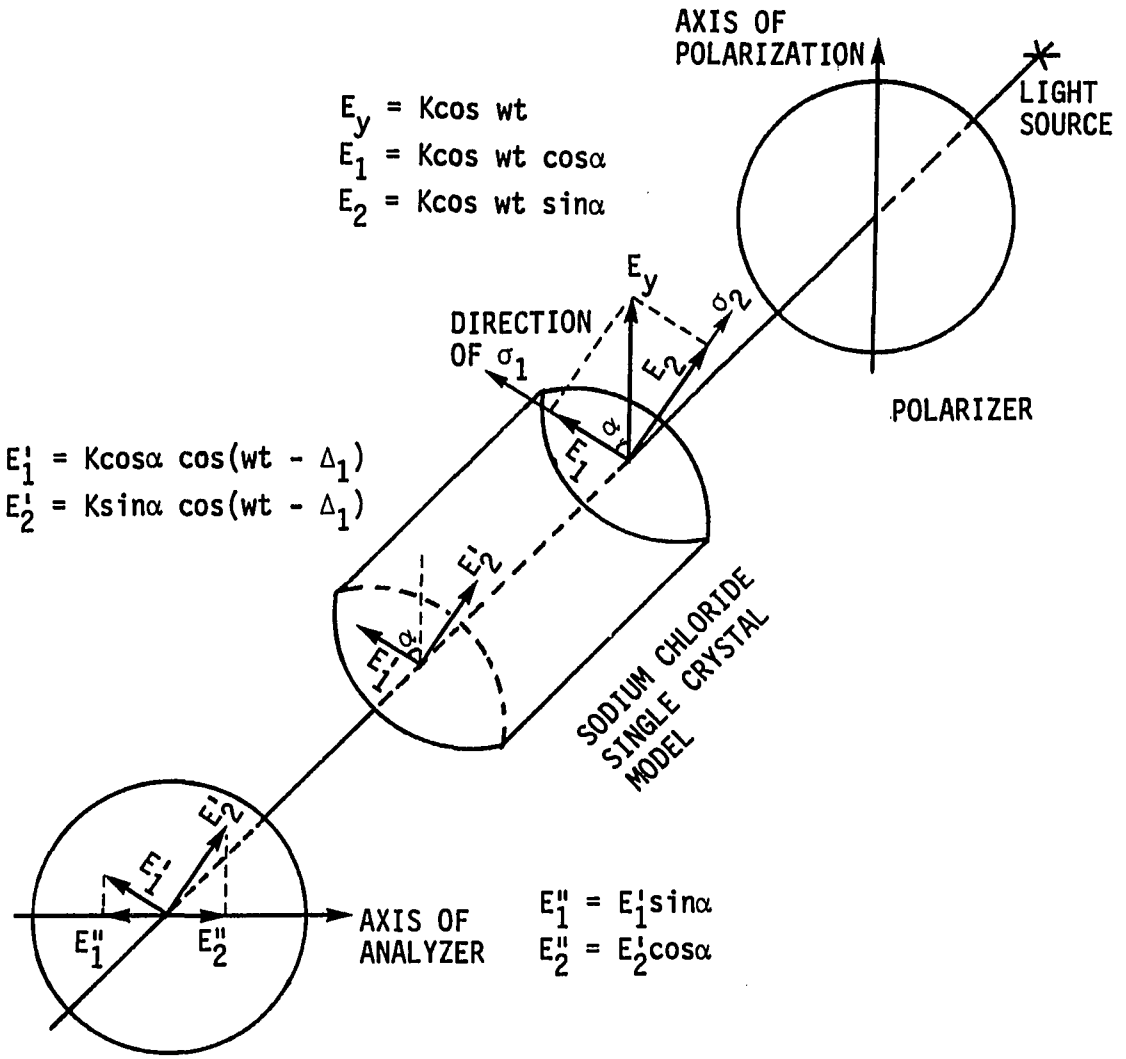

Figure 17. A stressed sodium chloride single crystal model in a plane polariscope

$$I = K \sin^2 2\alpha \sin^2 \frac{\pi hc}{\lambda} (\sigma_1 - \sigma_2) \quad . \qquad (30)$$

An examination of Eq. (30) indicates the following summary:

(1) For a given $(\sigma_1 - \sigma_2)$, when $\alpha = n \cdot 90° \pm 45°$, the highest light intensity $[I = K \sin^2 \pi hc/\lambda (\sigma_1 - \sigma_2)]$ occurs.

(2) When $\alpha = n \cdot \pi/2$, extinction $(I = 0)$ occurs.

Because everywhere near the slip line the principal stresses σ_1 and σ_2 are parallel and perpendicular to the slip line, according to the summary (1) above, we should see strong birefringence of slip line if slip line is 45° with the axis of the polarizer. This is exactly true. Figure 16 shows this result. We often see, at 45°, bright birefringent images of slip lines in sodium chloride single crystal when the axis of the polarizer is in a perpendicular direction. According to the summary (2) above, if the slip line is parallel or perpendicular to the axis of the polarizer, extinction occurs. This is also true in the birefringent experiments with sodium chloride single crystals.

The discussion above strongly shows that birefringence of slip lines in sodium chloride single crystals is the result of the stress fields of the slip line on which the dislocations piled up.

The uniqueness of the dislocation birefringence

Comparison between the photoelastic fringe patterns in photoelastic materials and the fringe patterns in sodium chloride single crystals (Figures 18 and 19) shows that they are quite different. We did not observe any isochromatic or isoclinic fringe patterns in

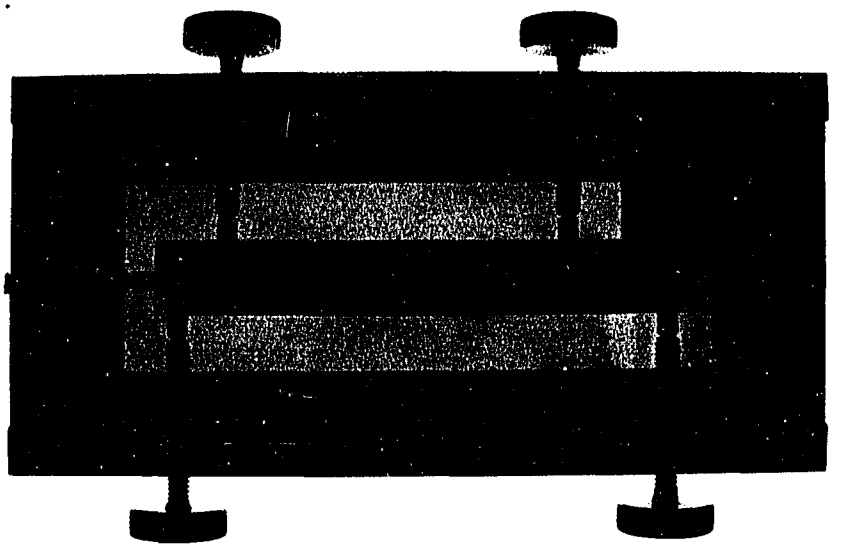

Figure 18. Isochromatic fringe patterns in photoelastic material in four-point bending

Figure 19. Photoelastic image of a sodium chloride single crystal in four-point bending

the sodium chloride single crystals. The only birefringent fringe patterns observed were caused by the 45° edge dislocation slip bands. These observations in sodium chloride single crystals are due to the pile up of dislocations. For a pile up of dislocations, the total force on the ith dislocation is given by [68]

$$\frac{Gb^2}{2\pi(1-\nu)} \sum_{\substack{j=0 \\ j\neq i}}^{n} \frac{1}{x_i - x_j} - \sigma b = 0 \qquad (31)$$

where

n = the number of dislocations piled up behind the lead dislocation, denoted by the subscript 0,

b = the component of the Burgers vector b_i of each of the dislocations,

G = shear modulus,

ν = Poisson's ratio,

σ = normal stress,

x_i = distance between obstacle and ith dislocation and

x_j = distance between obstacle and jth dislocation.

One of the most important results obtained from the solution of this equation is that the first dislocation experiences a combined stress, σ^*, arising from the presence of the other dislocations and the applied shear stress equal to

$$\sigma^* = n\sigma \quad . \qquad (32)$$

Also, there is a high magnitude of shear stresses at the head of the pile up. These high shear stresses make the previously existing pile up line extend easily. Figures 19 and 20 show this result. In Figure 19, even though the external loads are very small, the first 45° dislocation pile up line can be formed due to the stress concentration at each loading point. Figure 20 illustrates the small external load (p_1) and the first 45° edge dislocation pile up line AB of Figure 19. There is high shear stress at the head of pile up line AB due to the dislocation pile up AB. Therefore, any small external load increase (Δp) will make more dislocations move ahead of the line AB. This will create a formation of a new pile up group or a length increase of the piled up group. Therefore, the piled up line AB will expand along the AB direction. Based on the stress fields of this pile up line, a 45° birefringent image can be easily observed. The dislocation pile up described the configuration of dislocation distribution on the slip line. The slip line has a high density of dislocations. It is the high density of dislocations that gives the strong birefringence.

Because the dislocation pile up along AB line in Figure 20 allows plastic strain at low external load, the external load will be small when the plastic deformation takes place along AB. And due to this plastic deformation, the external load cannot reach a high value. Therefore, the stress anywhere away from the pile up line is small. Once the magnitude of the stress is low, a critical value of principal stress difference ($\sigma_1 - \sigma_2$) cannot be reached for a visible

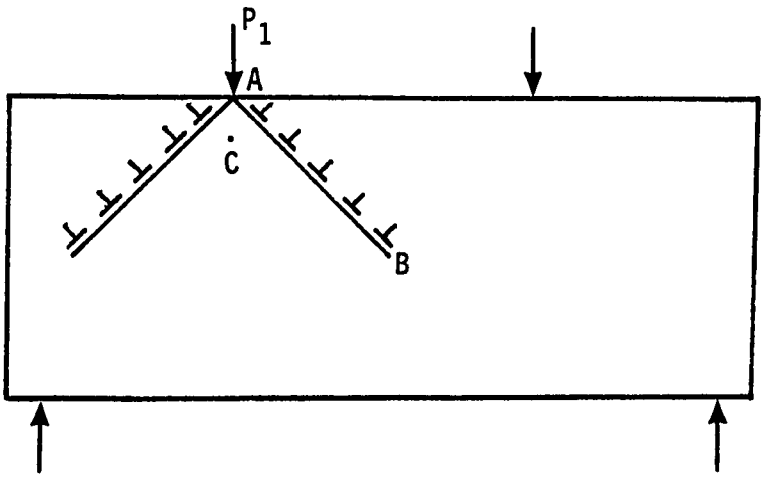

Figure 20. An edge dislocation pile up easily propagates along AB direction

birefringence with the photoelastic system which was used in this study. For example, at the point C of Figure 20, the stress is much lower at external load $p_1 + \Delta p$ as compared with the stress near the dislocation slip line AB. In the photoelastic materials, polymers $(\sigma_1 - \sigma_2)$ can be increased by increasing the external load. However, as we discussed above, in a sodium chloride single crystal, high stress at point C is difficult to reach. According to Eq. (15):

$$I = K \sin^2 2\alpha \sin^2 \frac{\pi hc}{\lambda} (\sigma_1 - \sigma_2) ,$$

if the $(\sigma_1 - \sigma_2)$ is small, birefringence at point C is invisible. We can only see the birefringence of the dislocation slip line which has a high value of $(\sigma_1 - \sigma_2)$. But after a serious plastic deformation and work hardening of the sample, maybe we can see some isoclinic fringe patterns between the slip bands. This situation should be avoided in the application of dislocation birefringence. To study the dislocation mechanisms of fracture, we hope to have the birefringence in sodium chloride single crystals to be the only one due to the dislocation movement. If the birefringence can be caused by sources other than dislocations, it will be difficult to determine the dislocation movement from the observation of birefringence.

To illustrate the relationship of dislocation slip band, photoelasticity and low magnitude of $(\sigma_1 - \sigma_2)$ caused by pile up, a test sample of {110} surface planes for four-point bending was

prepared (Figure 21). In Figure 21, we observed three different regions. These regions are shown schematically in Figure 22. Because the {110} planes are the surfaces of the sample, the shear stress in the regions of A and C of Figure 22 makes the edge dislocation slip (b = <110>) lined up from the top surface to the bottom surface. Therefore, the birefringent patterns of dislocation slip can be seen easily. However, in region B (pure tension and compression region of four-point bending), the normal tensional (or compressive) stress cannot push any dislocation to glide on the {011} planes and also the <100> Burgers vectors are not active on {100} planes. Therefore, there is no dislocation generation and movement. Hence, we cannot see the birefringent patterns of dislocation slip. Also, we cannot see the isochromatic and isoclinic fringe patterns in region B because $(\sigma_1 - \sigma_2)$ is very small. This small $(\sigma_1 - \sigma_2)$ is due to the plastic deformation in the regions A and C.

From the test results with sodium chloride single crystals, the birefringence is caused only by the dislocation slip bands. Therefore, the birefringence can be used to study the dislocation movement and dislocation mechanisms of fracture in sodium chloride.

Plastic zone shape in sodium chloride single crystals

Due to the elastic stress fields of dislocation slip lines, the slip bands can be observed by photoelasticity. Therefore, photoelasticity can help us to find the plastic zone in sodium chloride single crystals. To see the shape of a plastic zone at a crack tip of a

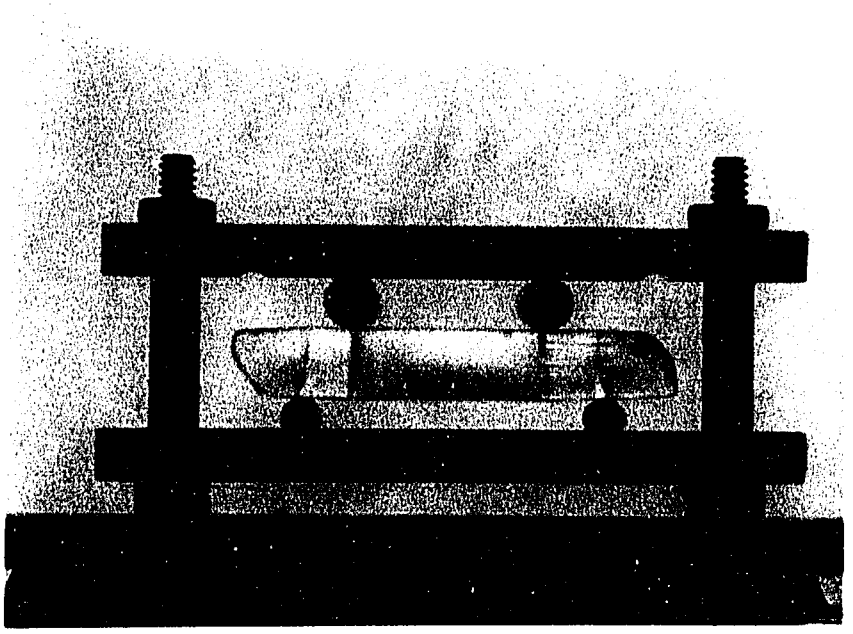

Figure 21. Four-point bending of a sodium chloride single crystal with surface planes {110} in plane polariscope

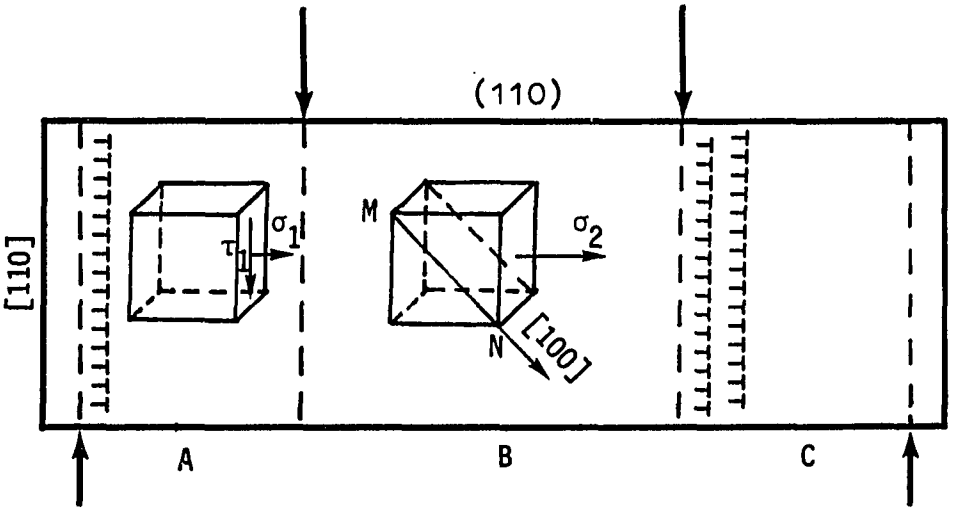

Figure 22. Dislocation movement of the sample in Figure 21

single crystal, a sample of 6 x 8 x 12 mm with a sharp <100> notch was prepared. This sharp V-notch was made with a string saw to prevent damage by conventional machining. The sample was tested in four-point bending (Figure 23). The load-deflection relationship is shown in Figure 24. Figure 23 shows that when the load increases in four-point bending, the dislocation slip bands develop from O along 45° OM and ON directions. When the load of Figure 24 reaches near point O, the dislocation slip bands of Figure 23 can develop from point O to the point R and S on the top surface. If the load is high, second slip bands OT and OV, or more slip bands can be formed. These slip bands give the plastic zone at the V-notch tip. When the load of Figure 24 reaches point O, a new crack OA (Figure 23) propagates suddenly from O to A. This new crack drops the load down from point O in Figure 24 to point A. If the load increases again from A to B in Figure 24, a second new plastic zone at the crack tip A in Figure 23 will form again (see dislocation slip lines AP and AQ in Figure 23). Obviously, this plastic zone is not a butterfly shape as shown in Figure 25. The plastic zone in sodium chloride single crystals always develops along active slip bands. Because the plastic deformation can occur along the slip direction under a small external load and this plastic deformation made the stress magnitude small anywhere away from the slip bands, it is impossible to form the butterfly plastic zone of Figure 25 in single crystals [69]. However, in a polycrystal, the grain boundaries can stop the pile up. Therefore, a butterfly plastic zone can be formed in fine grained polycrystalline materials, but this

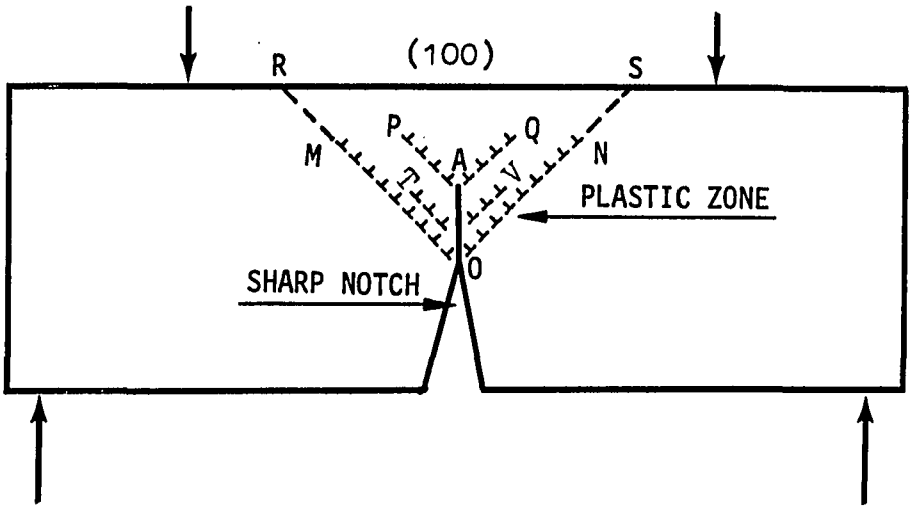

Figure 23. Plastic zone of a sodium chloride single crystal with <100> cleavage crack

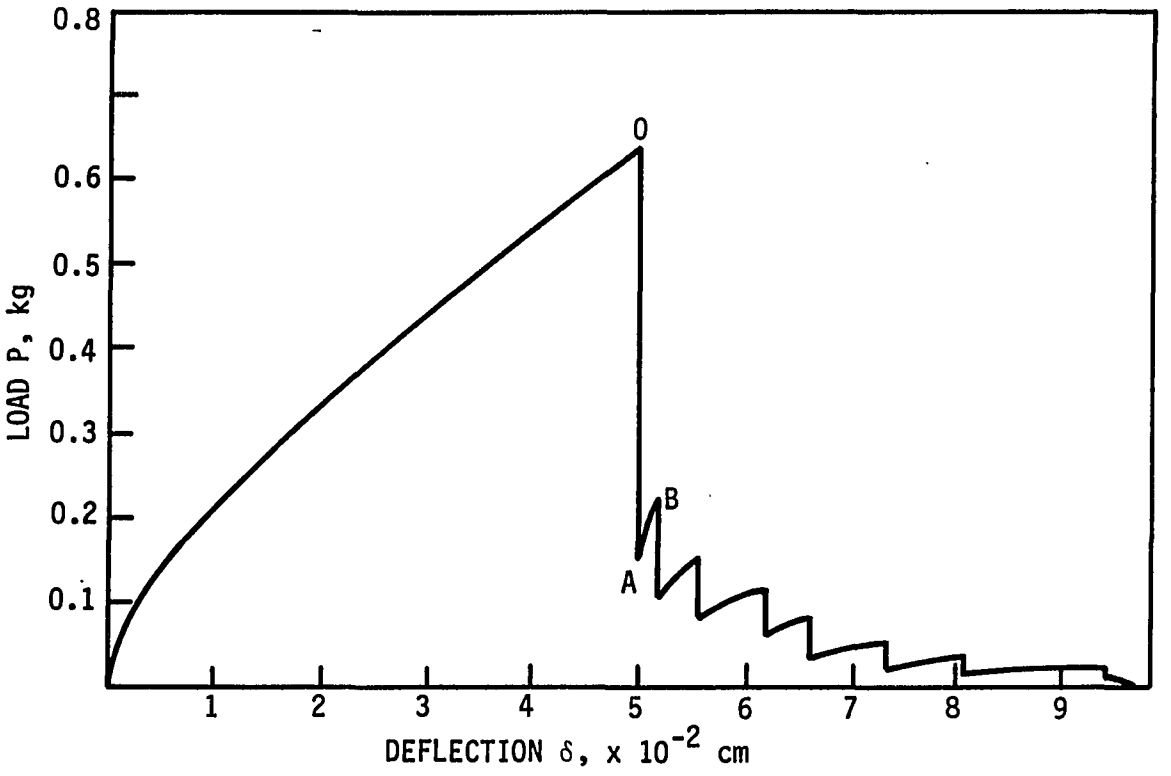

Figure 24. Load-deflection curve of a sodium chloride single crystal with a sharp V-notch. The load drop from O to A in Figure 24 corresponds to the new crack OA propagating from O to A in Figure 23

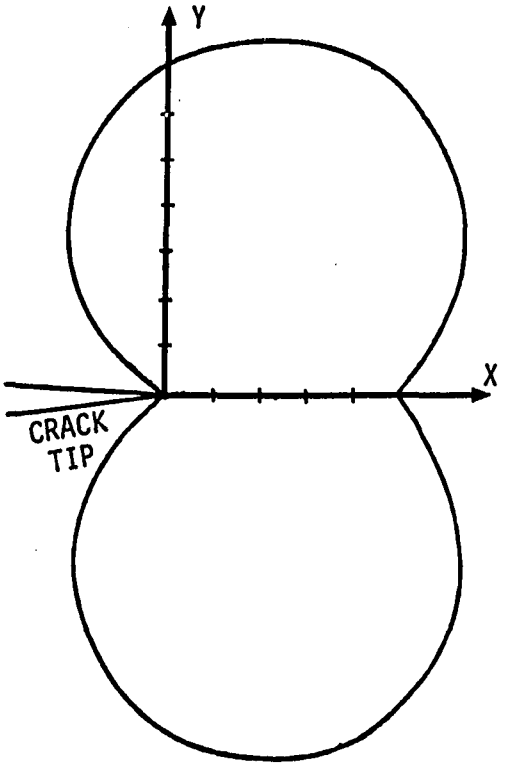

Figure 25. Plastic zone shape at the crack tip in a through-the-thickness crack in a plane according to the theoretical model

will reduce the fracture toughness. In other words, single crystals can demonstrate a better ductility than polycrystals.

Figure 26 illustrates another type of notch which is not in {100} planes, but {110} planes. The plastic zone for this <110> notch was shown in Figure 26. Figure 27 is the photoelastic fringe patterns taken from the polariscope with <110> notch 45° from the axis of polarization. The bright region in Figure 27 is conformed to the dislocation slip bands (i.e., plastic zone) in Figure 26. The plastic zone at the crack tip for <110> notch is not a butterfly shape. It is also different from the <100> notch shown in Figure 23.

In this section, the birefringence has been discussed. The purpose for studying the birefringence in sodium chloride is to know the dislocation mechanisms of the fracture. An understanding of the dislocation mechanisms of fracture is very important in measuring the fracture toughness parameters. More discussion of the birefringence and dislocation mechanisms of fracture will made in the next section.

Measurement of Work of Fracture

Unstable fracture of ductile body

The three-point bending experiments were conducted at a cross-head speed of 0.0005-0.002 cm/min. in different temperatures. Only at liquid N_2 temperature, for a brittle or a semibrittle fracture, could the fully stable crack propagation be obtained (Figure 10). At room temperature, the sodium chloride single crystals appear to be ductile.

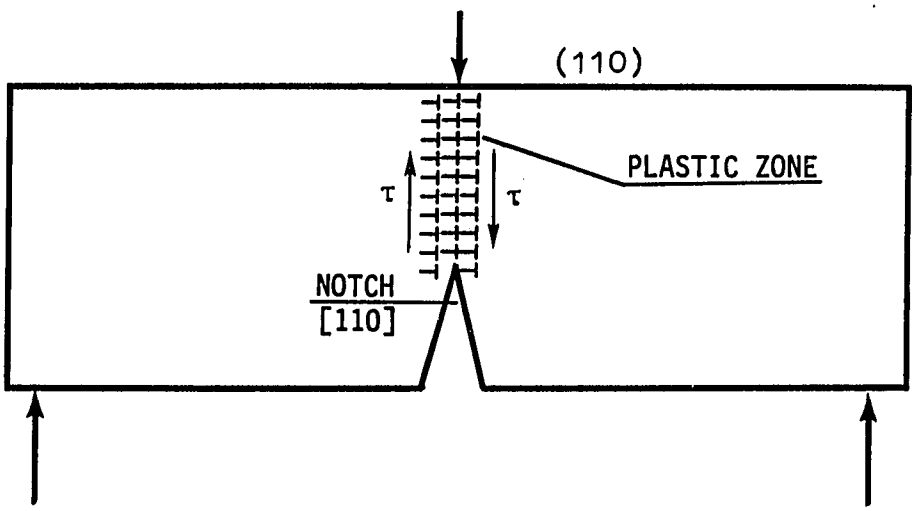

Figure 26. Plastic zone of a notch propagating in the <110> in a sodium chloride single crystal

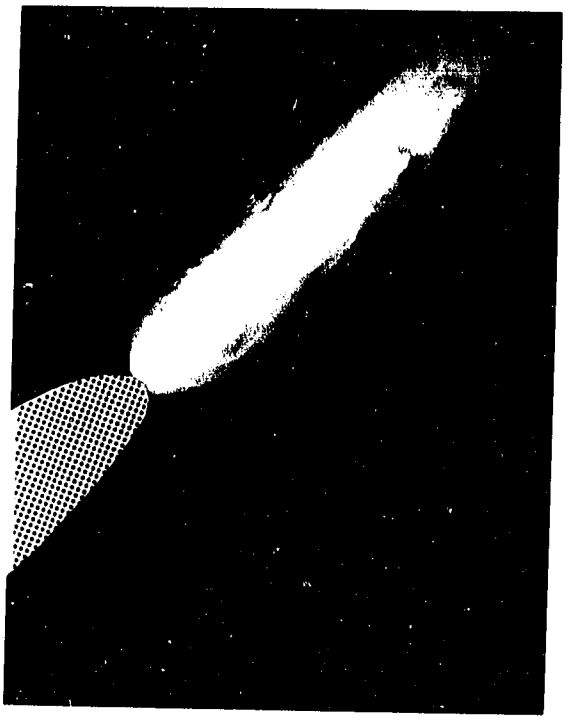

Figure 27. Photoelastic image of plastic zone in a sodium chloride single crystal with <110> notch rotated clockwise 45° from the orientation shown in Figure 26

In a ductile condition due to a high plastic energy dissipation at the crack tip, a fully stable crack propagation is impossible.

Figure 28 illustrates the load (p) vs deflection (δ) curve for this unstable crack propagation. In Figure 28, only a very short straight line, OA', can be seen. The plastic deformation began from point A' at a very small load (p'). This is due to dislocation movement which can easily cause plastic deformation at a small external load. The plastic deformation at the crack tip leads to a crack tip blunting, i.e., CTOD increases. It also leads to work hardening at the plastic zone of the crack tip. The shape of the curve A'A is due to both crack tip opening and work hardening. The crack tip blunting made it possible for the sample, which was sharply and deeply notched, to withstand a large external load, P_A. This large external load, P_A, will cause a very large increase in the elastic stored energy of the sample. This can be seen from curve OA'A of Figure 28. In Figure 28, OA' is a short linear elastic line that is similar, but shorter as compared with the linear elastic line in Figure 10. This phenomena can be explained as follows. Comparing the samples in Figures 10 and 28, the sample in Figure 10 can be considered as the sample without crack tip opening. The stress at the crack tip of the sample in Figure 10 is near the fracture stress (σ_f). Usually, σ_{yield} stress is less than σ_f. Therefore, the yield stress (σ_{yield}) of the sample in Figure 28 should be less than σ_f. Furthermore, dislocation pile up can cause the sample to yield at a lower load, so the load p' at point A' in Figure 28 should be very small. In other words, OA' of Figure 28 is

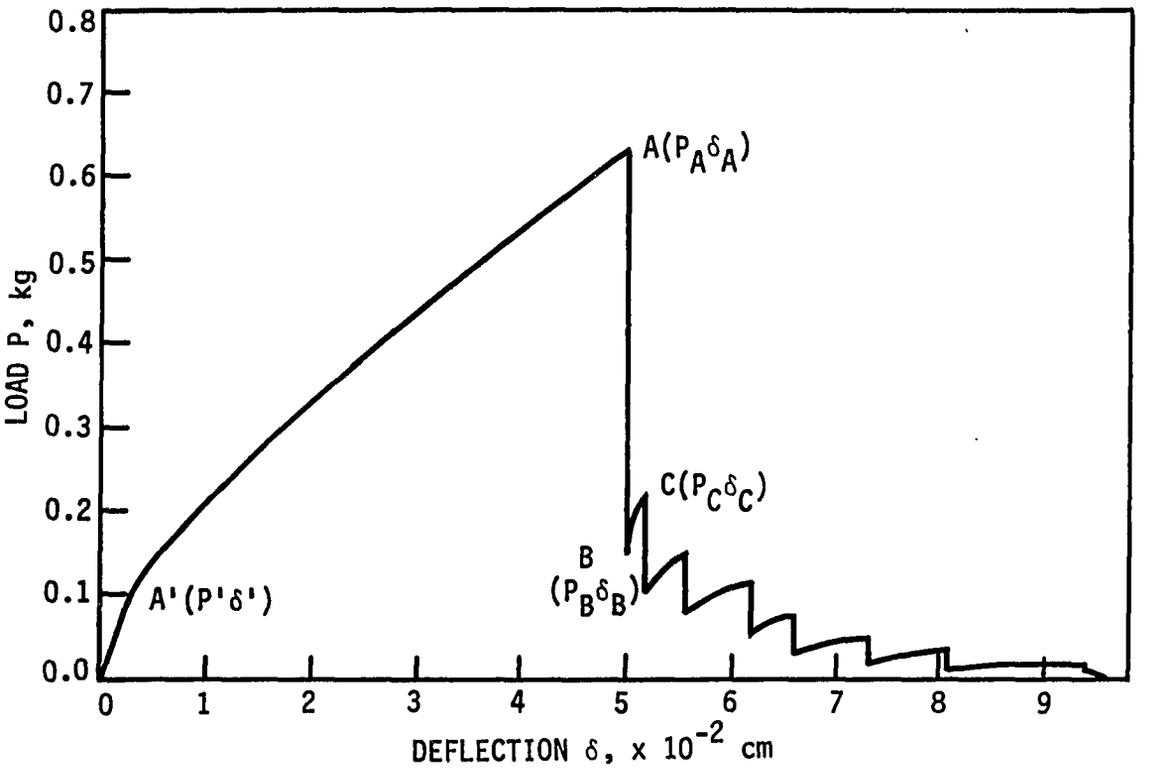

Figure 28. Load (p) vs deflection (δ) curve for temperature 22°C and cross-head speed 0.0005 cm/min

much shorter than the linear elastic line in Figure 10. Because OA' is very short, the stored elastic energy is very small at point A'. This stored elastic energy can be measured by constructing a right angle triangle with hypotenuse OA'. The elastic stored energy in the sample at the point A can be measured in the same way as above with a right angle triangle with its hypotenuse - the unloading path from point A. Obviously, point A has a higher elastic stored energy than point A' (but in comparison with plastic energy dissipation, this increase of elastic energy is still small). Once the plastic zone at the crack tip cannot extend more or deform more at a certain value of load, there will be an unstable crack propagation because

$$-\frac{d(U_S + U_M)}{dc} > \frac{dW_{wof}}{dc} \quad . \tag{33}$$

As unstable crack propagation occurs, the external load drops down from P_A to P_B (Figure 28). For this unstable crack propagation, the elastic energy release can be calculated from the compliance change of the sample. The released elastic stored energy in the sample was spent for both the surface energy of the newly formed surface and the kinetic energy loss of the unstable fracture. This pattern of crack opening (curve OA) and propagation (line AB) was repeated under constant test speed. Figure 28 clearly shows that a few steps of crack tip opening with work hardening, followed by an unstable crack propagation, can appear until total failure occurs. If the kinetic energy loss is

negligible for each crack propagation in Figure 28, the work of fracture can be calculated from Eq. (25).

Variable parameters of work of fracture

For a given material, the work of fracture is dependent on the stress condition, the strain rate and the temperature. For a fracture in a plane stress condition, the work of fracture is much larger than in a plane strain condition. Figure 29 illustrates the work of fracture in a plane stress condition. It has a larger value when compared with Figure 28, which was in a plane strain condition. Usually, a plane strain condition leads to a triaxial state of stress. These triaxial stresses reduce the shear stress on the slip plane. Therefore, it is difficult to make dislocations to move. In this case, the tested sample could not absorb much plastic deformation energy. It becomes brittle.

The measurement of work of fracture shows that the work of fracture in a high strain rate condition is less than in a low strain rate condition. This is because the high strain rate forces the dislocation to move without enough time, i.e., the dislocation could not move at high strain rate. But at a low rate of loading, the dislocation can move with lower speed, and thus, the work of fracture can be increased.

The temperature effects on work of fracture are illustrated in Figure 30. The p-δ curves for T = 250°C and T = 22°C were compared. The p-δ curve for T = 250°C has a bigger first crack propagation (from point A_3 to point B_3) than for T = 22°C (from point A_2 to point B_2).

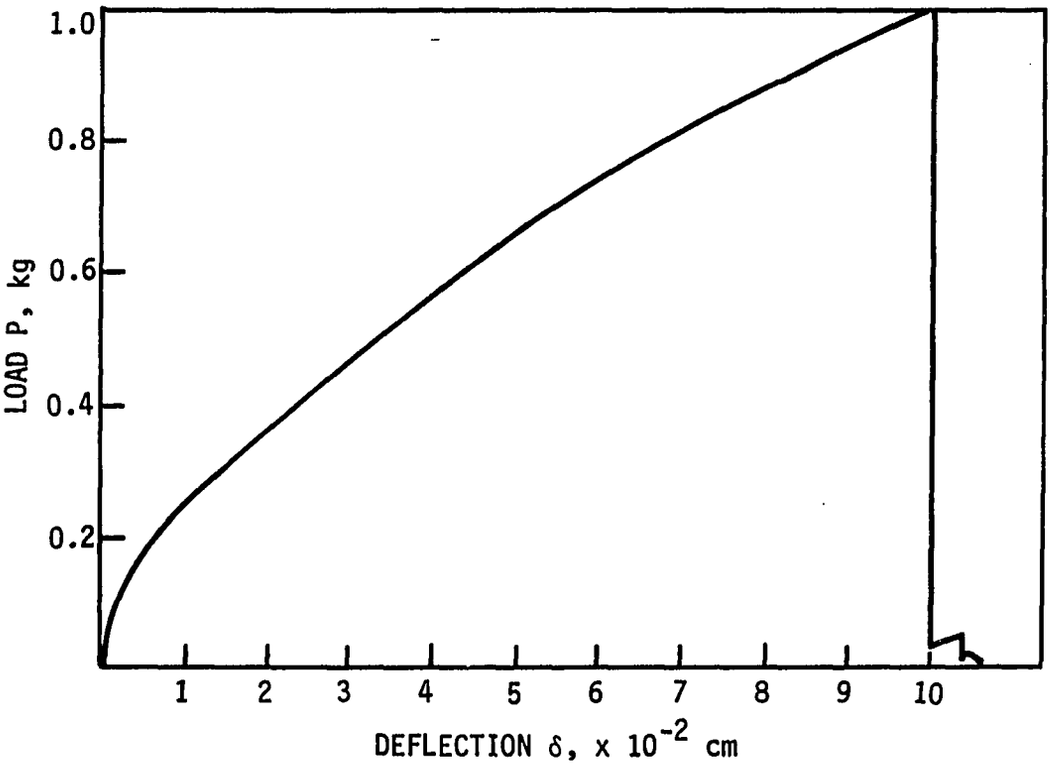

Figure 29. Load (p) vs deflection (δ) curve for temperature 22°C and cross-head speed 0.0005 cm/min in plane stress condition

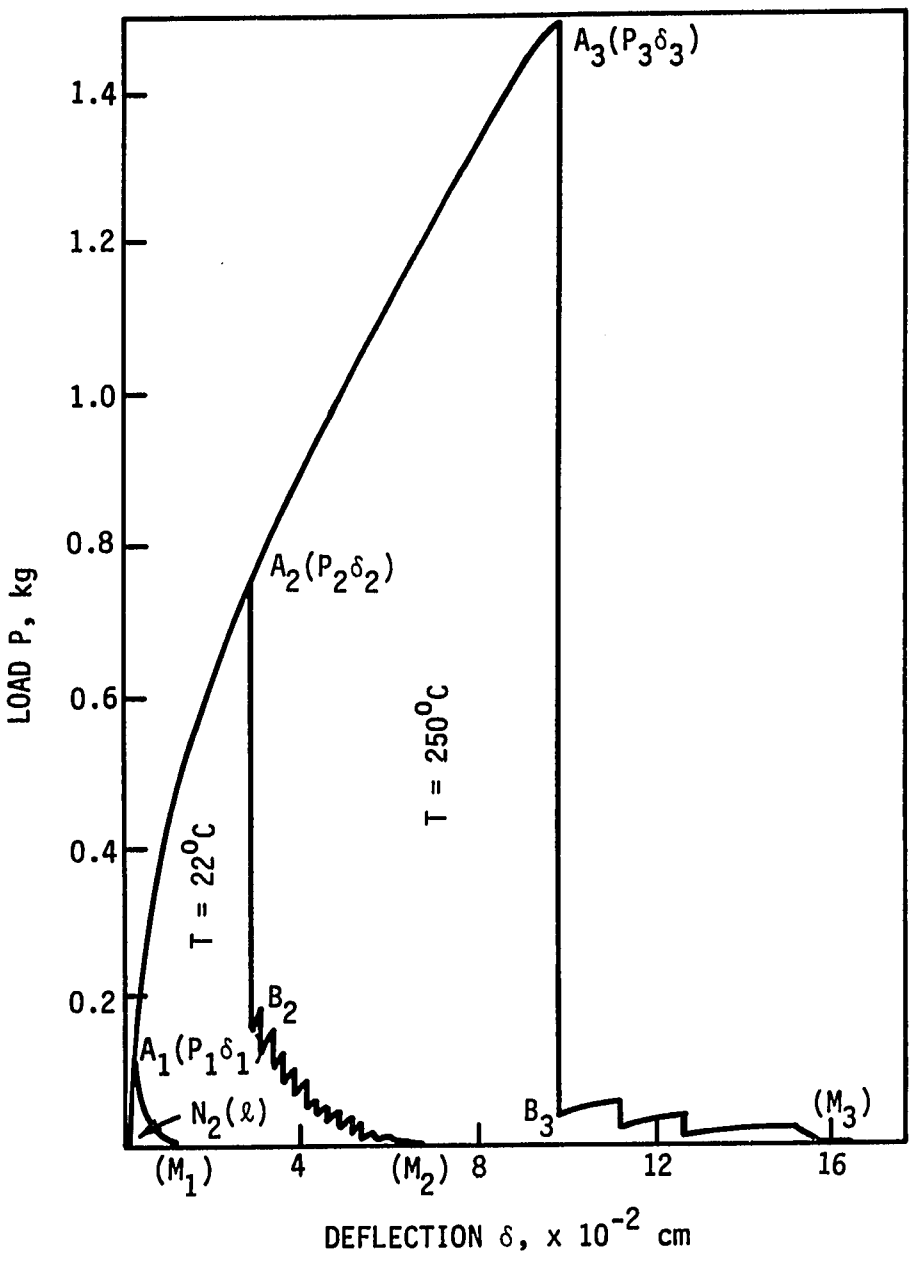

Figure 30. Load (p) vs deflection (δ) curves for different temperatures indicating the transition from linear elastic fracture to elastic-plastic fracture and ductile fracture

Once the temperature reaches greater than T = 250°C, a large CTOD value allows the sample to withstand a much larger external load. An extreme elastic stored energy due to this external load will result in sudden total failure. When the temperature is lowered to liquid N_2 temperature, a fully stable and very slow crack propagation can be achieved.

Figure 30 indicates that the higher the temperature, the bigger the first maximum load and the larger the integral area. These results may be due to the following reasons:

(1) A new slip system occurs at an elevated temperature. For example, at room temperature, the slip planes in sodium chloride are {110}. At high temperatures, {100} slip planes are possible [70].

(2) The thermally activated processes increase ductile behavior [71]. According to the theory of the thermally activated deformation, the internal resisting stresses can be grouped into two categories: a) long-range obstacles to plastic deformation, which represent barriers too high and long to be surmounted by thermal fluctuation and b) short-range obstacles, less than 10 atom diameters for which thermal fluctuations can assist dislocations in surmounting these barriers. Thus, the thermally activated processes can assist deformation and reduce flow stress at elevated temperature. The temperature dependence of flow stress at constant strain and strain rate generally can be represented by

$$\sigma_s = C\, e^{\Theta/RT}\Big|_{\varepsilon,\dot{\varepsilon}} \qquad (34)$$

where

Θ = an activation energy,

R and C = constants,

T = temperature and

σ_s = flow stress.

When T increases, σ_s decreases. Therefore, at high temperature, the tested sample becomes ductile.

(3) At high temperature, the velocity of a dislocation increases. The velocity of a dislocation can be expressed by [72]

$$\nu = f(\sigma)\ e^{-E/KT} \tag{35}$$

where

σ = applied stress,

T = temperature,

ν = velocity of dislocation,

K = constant and

E = activation energy.

Obviously, the ν increases with increasing of temperature. Therefore, a high temperature leads to good ductility.

(4) Dislocation climb and atomic diffusion are possible. These also lead to a good plastic behavior.

Figure 30 also indicates both the integral area and the first maximum load, just before the first crack propagation, can be used to

determine the transition temperature of brittle-ductile fracture. The maximum loads (P_1, P_2, P_3) in Figure 30 are related to the crack tip open distance (CTOD). The CTOD is a measurement of plastic zone size and plasticity of plastic zone which is affected by temperature as we discussed above. The integral area is related to the work of fracture. There is a kinetic energy loss for each step of unstable crack propagation. But in comparing this kinetic energy loss to the energy loss in an impact test or a small punch test [73], this kinetic energy loss is negligible. Impact tests and small punch tests are often used to measure the transition temperature. As compared to the conventional tests above, the work of fracture test and the maximum load test can be considered as quantitative physical parameters for transition temperature measurement because they are closely related to the fracture toughness parameters.

Figure 31 shows a part of the p-δ curve of three-point bending for a sodium chloride single crystal at room temperature. In Figure 31, the load drop from A to B corresponds to a crack propagation Δa which has a new crack surface ΔA. The photoelastic observation of dislocation movement shows that the plastic deformation is negligible in this propagation process of crack. In other words, for this propagation process, the sample can be considered as a linear elastic body. There is an elastic energy release due to the crack propagation. In this crack propagation, the external work input is zero. The energy necessary for the newly cracked surface, resulting from the crack propagation, is delivered entirely by the elastic energy release.

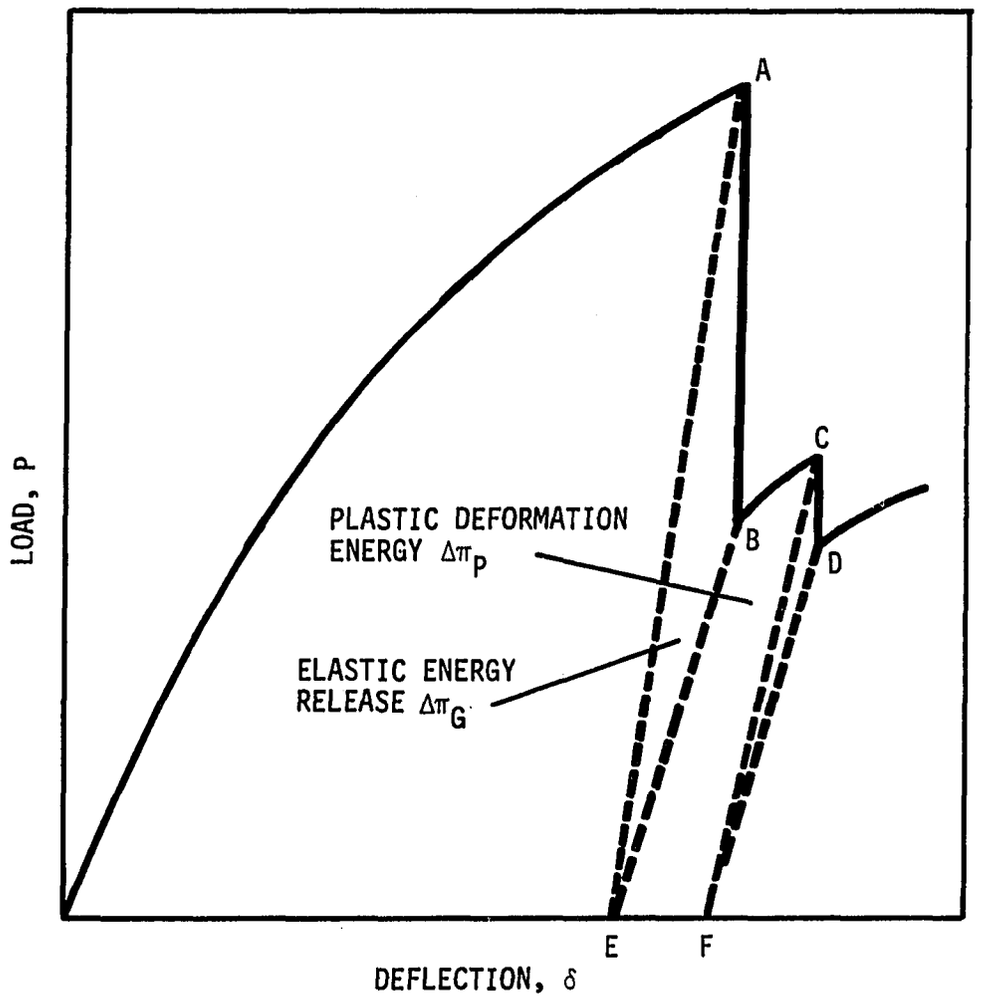

Figure 31. The plastic energy dissipation rate and the elastic energy release rate in a ductile fracture

It is different from the constant load test in which the surface energy is delivered by the external force.

We can unload the sample from B to E (Figure 31). When this is done, it does not display any visible degree of rehealing or plastic deformation based on examination of the shape of the unloading path [74]. Only at the beginning of unloading from B to E, the trace of p-δ unloading path is curved slightly. This is probably due to the recovery of some piled up dislocations. Even though the trace BE of the unloading path is not exactly a straight line, it can be approximately simplified to be a straight line BE. By connecting points A and E, the area $\Delta\pi_G$ enclosed within the region ABE is the elastic energy release due to the compliance change. For any crack growth in a test sample, the total energy balance can be written as [56]:

$$\frac{\partial w}{\partial A} = \left(\frac{\partial U_e}{\partial A} + \frac{\partial U_p}{\partial A}\right) + \frac{\partial \Gamma}{\partial A} + \frac{\partial W_{KE}}{\partial A} \qquad (36)$$

where

A = increment of the cracked surface area,

w = work input by the external force,

U_e = elastic energy of the sample,

U_p = plastic energy dissipation,

Γ = newly cracked surface energy and

W_{KE} = kinetic energy loss with the crack propagation.

By applying Eq. (36) to the crack propagation in which the load, p, drops from point A to point B in Figure 31, using $\partial w/\partial A = 0$ and $\partial U_p/\partial A \doteq 0$, then Eq. (36) becomes

$$\frac{-\partial U_e}{\partial A} = \frac{\partial \Gamma}{\partial A} + \frac{\partial W_{KE}}{\partial A} \quad . \tag{37}$$

In Eq. (37), $-\frac{\partial U_e}{\partial A}$ is the elastic energy release rate or the crack driving force, G. It can be expressed

$$G = \frac{\Delta \pi_G}{\Delta A} \quad . \tag{38}$$

As we discussed previously, after the crack propagation, the new cracked tip will be blunted if a constant cross-head speed is maintained. This crack blunting is also called crack opening of the new cracked tip. The trace BC in Figure 31 illustrates the work hardening and crack tip opening. Once the work hardening reaches some critical value (point C), a second crack propagation will occur again. The CF line can be constructed by drawing an unloading line, DF. BE is nearly parallel to CF. The area $\Delta \pi_p$ enclosed within the region EBCF is equal to plastic deformation energy dissipation due to the plastic deformation at the crack tip. For this crack opening from B to C, the elastic energy also increases, but it is very small as compared with the plastic energy dissipation. This elastic energy will always be released for the next crack propagation. There is no new cracked

surface during this crack opening (i.e., path BC). Based on the existence of the first cracked surface ΔA, for the path EBCF, we may write $\partial U_e/\partial A = 0$, $\partial \Gamma/\partial A = 0$ and $\partial W_{KE}/\partial A = 0$. Then, Eq. (36) becomes

$$\frac{\partial w}{\partial A} = \frac{\partial U_p}{\partial A} \tag{39}$$

or

$$\frac{\partial w}{\partial A} = \frac{\partial U_p}{\partial A} = \frac{\Delta \pi_p}{\Delta A} = \phi_p \quad . \tag{40}$$

In Eq. (40), ϕ_p is defined as a plastic deformation energy dissipation rate. Because the elastic energy increment in path BC is small enough to ignore, Eqs. (39) and (40) are also suitable for path BC. Therefore, in the crack open process, the work input by the external force is almost entirely plastic deformation energy dissipation.

In a three-point bending test at a slow test speed, ductile rupture includes many steps of crack opening followed by crack propagation. The plastic deformation energy was dissipated by crack opening processes at the crack tip. Crack propagation will release the elastic energy which is dissipated as cracked surface energy and as kinetic energy. Because the crack tip opening has resulted in extra elastic stored energy, it is impossible to get a stable fracture in a ductile body as we discussed before.

Stable fracture of elastic-plastic body

When the temperature is reduced, the crack tip opening is more difficult. Hence, an elastic-plastic body can be obtained. For this semibrittle body, the extra elastic stored energy no longer exists. Therefore, a fully stable crack propagation can be obtained. Figure 32 is a typical p-δ curve for a fully stable fracture. For this fully stable crack propagation, the process of fracture is the same as in the ductile body. We also can separate the total fracture energy into two parts - newly cracked surface energy and plastic energy at the crack tip. In the p-δ diagram of Figure 32, the AC and BD are the unloading paths. From point A to point B, the crack propagation is assumed to be Δa and the corresponding newly cracked surface is assumed to be ΔA.

To analyze the crack propagation, let us take point C as an initial state. At point C, the sample has a plastic strain energy, U_{pc}, and the residual elastic energy is assumed to be zero. Point D was suggested to be the final state of the path CABD. At point D, the sample has a plastic strain energy, U_{pD}, and the residual elastic energy is also assumed to be zero. A residual plastic deformation, $\Delta\delta_p$, is left behind due to the plastic deformation at the crack tip. The work input by the external force is the area $\Delta\pi_R$ enclosed within the region CABD. Since the crack velocity is very small, the kinetic energy loss of the sample is negligible. Thus, the energy balance in a fully stable propagation can be written as

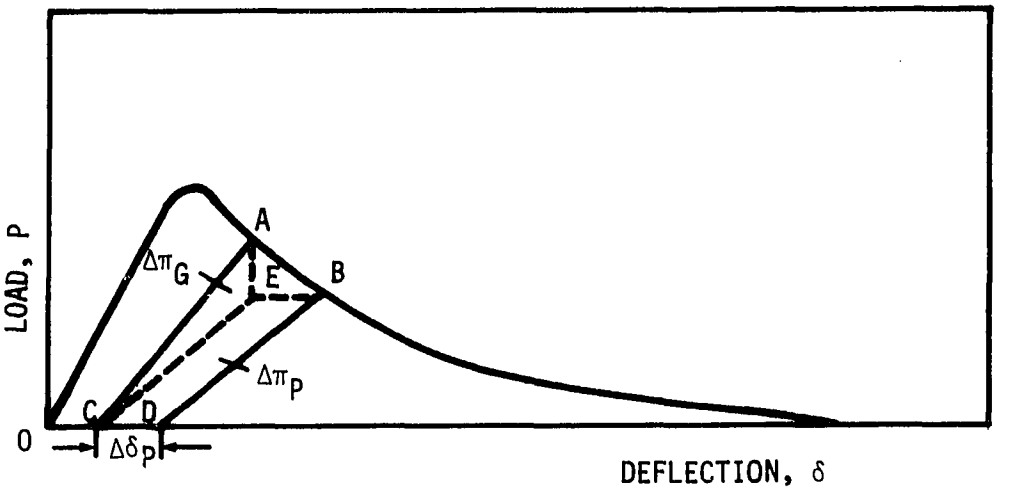

Figure 32. Loading and unloading paths for elastic-plastic body with a stable fracture

$$\frac{\partial w}{\partial A} = \left(\frac{\partial U_e}{\partial A} + \frac{\partial U_p}{\partial A}\right) + \frac{\partial \Gamma}{\partial A} \quad . \tag{41}$$

In Eq. (41), $\partial U_e/\partial A = 0$ for the path from initial state to final state. Then, Eq. (41) becomes

$$\frac{\partial w}{\partial A} = \frac{\partial U_p}{\partial A} + \frac{\partial \Gamma}{\partial A} \quad . \tag{42}$$

In Figure 32, the line CE was drawn parallel to BD. The perpendicular line AE was drawn to cross CE at point E. Connect point E and B. Thus, the stable fracture path AB is substituted by AE and EB which are, respectively, the equivalent unstable crack propagation and crack tip opening. In comparing Figures 31 and 32, the area $\Delta\pi_G$ enclosed within the region CAE in Figure 32 can be considered as elastic energy release. The area $\Delta\pi_p$ enclosed within the region CEBD can be considered as plastic energy dissipation at the crack tip. Both Figures 31 and 32 illustrate the same processes of fracture.

In fact, the stable fracture path AB in Figure 32 consists of a number of steps of crack tip opening followed by crack propagation. Equations (37) and (38) show

$$G = \frac{\Delta\pi_G}{\Delta A} = \frac{\Delta\Gamma}{\Delta A} + \frac{\Delta W_{KE}}{\Delta A} \quad . \tag{43}$$

Equation (43) shows that

$$\Delta\pi_G > \Delta\Gamma \quad . \tag{44}$$

In other words, for the unstable crack propagation of path AE of Figure 32, the newly cracked surface energy cannot be more than $\Delta\pi_G$ (only based on the configuration of Figure 32). On the other hand, the line EB in Figure 32 looks like an ideal plastic deformation line without work hardening and crack tip opening. Therefore, a correction should be made for considering both work hardening and crack tip opening. The CEABDC which is the difference of $\Delta\pi_R$ and $\Delta\pi_G$ can be approximately taken as a corrected $\Delta\pi_p$. Equation (42) is rewritten as

$$\frac{\Delta w}{\Delta A} = \frac{U_{pD} - U_{pC}}{\Delta A} + \frac{\Delta \Gamma}{\Delta A} \tag{45}$$

where

$$\frac{\Delta w}{\Delta A} = \Delta\pi_R \tag{46}$$

$$\frac{U_{pD} - U_{pC}}{\Delta A} = \phi_p = \frac{\Delta\pi_p}{\Delta A} \tag{47}$$

$$\frac{\Delta \Gamma}{\Delta A} = \frac{\Delta\pi_G}{\Delta A} = G \quad . \tag{48}$$

The $G + \phi_p$ is defined as crack growth resistance (R). It can be written as

$$R = G + \phi_p = \frac{\Delta\pi_G}{\Delta A} + \frac{\Delta\pi_p}{\Delta A} = \frac{\Delta\pi_R}{\Delta A} \quad . \tag{49}$$

If $\Delta\pi_p$ is zero, $\Delta\pi_R = \Delta\pi_G = G$. Then, the sample would be a linear elastic body. The fracture of this body would be brittle. In this case, the work of fracture is the fracture surface energy.

The work of fracture can be obtained from the p-δ curve in Figure 10 by using Eq. (25):

$$W_{wof} = \frac{\int_o^{\delta_f} p d\delta}{2A_c} \quad . \tag{50}$$

Figure 10 is the stable crack propagation for a sodium chloride single crystal in liquid N_2. The work of fracture calculated from this figure is W_{wof} = 1100 ergs/cm^2. Figures 10 and 32 are the same p-δ curve. The loading and unloading paths in Figure 32 show that at liquid N_2 for cross-head speed 0.002 cm/min, the fracture of sodium chloride single crystal is a semibrittle fracture.

CONCLUSIONS

The results of this investigation lead to the following conclusions:

(1) Isoclinic fringe patterns and isochromatic fringe patterns could not be seen in sodium chloride single crystals when using the conventional photoelastic system in these experiments.

(2) The birefringent image which can be seen in the slip bands of sodium chloride single crystals is the birefringence of edge dislocation slip lines.

(3) Due to the conclusions above, the birefringent image in sodium chloride single crystals can be used to study the plastic zone at a crack tip, and the dislocation mechanisms of the fracture.

(4) The plastic zone shapes at a crack tip of a sodium chloride single crystal for either an <001> notch or a <110> notch are quite different from the expected plastic zone shape based on elastic stress field calculations.

(5) In three-point bending, at a slow test speed, fully stable fracture is impossible for a ductile body. The fully stable crack propagations can be obtained from an elastic-plastic body or a linear elastic body.

(6) As compared to impact testing and small punch testing, the kinetic energy loss is negligible in the measurement of work of fracture. The work of fracture and maximum load can be considered as a quantitative physical parameter for transition temperature

measurements. They approach closer to the fracture toughness parameters.

(7) Three-point bending with unloading paths can be used to calculate the crack driving force, plastic energy dissipation, crack propagation resistance, work of fracture and brittle-ductile transition.

(8) The work of fracture of sodium chloride at liquid nitrogen temperature was found to be plastic-elastic and had a value of 1100 ergs/cm^2.

BIBLIOGRAPHY

1. D. Broek, Elementary Engineering Fracture Mechanics, 3rd ed. (Martinus Nijhoff Publishing, The Hague, 1982), Chapter 1.

2. S. T. Rolfe and J. M. Barson, Fracture and Fatigue Control in Structures (Prentice-Hall, Englewood Cliffs, New Jersey, 1977), Chapter 1.

3. T. Bishop, Metal Progress 67, 79 (1955).

4. S. A. Long and T. D. McGee, J. Am. Ceram. Soc. 46, 583 (1963).

5. A. E. Wing and W. Rosenhain, Phil. Trans. Roy. Soc. (London) A193, 353 (1889).

6. D. Hull, Introduction to Dislocations, 2nd ed. (A. Wheaton & Co., Ltd., Exeter, 1975), p. 14.

7. E. Orowan, Z. Phys. 89, 604, 634 (1934).

8. M. Polanyi, Z. Phys. 89, 660 (1934).

9. G. I. Taylor, Proc. Roy. Soc. (London) A145, 362 (1934).

10. R. Peierls, Proc. Phys. Soc. 52, 34 (1940).

11. F. R. N. Nabarro, Proc. Phys. Soc. 59, 256 (1947).

12. J. Friedel, Dislocations, 2nd ed. (Pergamon Press, Ltd., Great Britain, 1967), Preface XVii.

13. W. T. Read, Dislocation in Crystals (John Wiley & Sons, Inc., New York, 1953).

14. A. H. Cottrell, Dislocation and Plastic Flow in Crystal (Oxford University Press, Oxford, 1953).

15. G. E. Dieter, Mechanical Metallurgy, 2nd ed. (McGraw-Hill, New York, 1976), p. 137.

16. S. Nourbakhsh and J. J. Crowther, Acta Met. 33, 1187 (1985).

17. J. J. Gilman and W. G. Johnston, J. Appl. Phys. 27, 1018 (1956).

18. D. Hull, Introduction to Dislocations, 2nd ed. (A. Wheaton & Co., Ltd., Exeter, 1975), p. 37.

19. J. C. Fisher, W. G. Johnston, R. Thomson and T. Vreeland, Dislocations and Mechanical Properties of Crystal (John Wiley & Sons, Inc., New York, 1957), p. 116.

20. S. A. Long, M.S. thesis, Iowa State University, 1962.

21. S. Amelinckx, Acta Met. 6, 34 (1958).

22. S. Amelinckx, J. Appl. Phys. 29, 1610 (1958).

23. J. W. Edington, Practical Electron Microscopy in Materials Science (N. V. Philips Gloeilampenfabrieken, Eindhoven, 1975), Monograph 3.

24. J. W. Menter, Proc. Roy. Soc. (London) A236, 119 (1956).

25. D. Hull, Introduction to Dislocations, 2nd ed. (A. Wheaton & Co., Ltd., Exeter, 1975), p. 41.

26. C. E. Hall, Introduction to Electron Microscopy (McGraw-Hill, New York, 1953), Chapter 10, p. 279.

27. D. C. Joy, D. E. Newbury and D. L. Davidson, J. Appl. Phys. 53, R81 (1982).

28. P. Morin, M. Pitaval, D. Bernard and G. Fontaine, Philos. Mag. A 40, 511 (1979).

29. J. I. Goldstein, D. E. Newbury, P. Echlin, D. C. Joy, C. Fiori and E. Lifshin, Scanning Electron Microscopy and X-Ray Microanalysis (Plenum Press, New York, 1981), Chapter 3, p. 120.

30. J. B. Newkirk, Phys. Rev. 110, 1465 (1958).

31. A. R. Lang, Acta Met. 5, 358 (1957).

32. A. R. Lang, J. Appl. Phys. 30, 1748 (1959).

33. A. R. Lang, Acta Cryst. 12, 249 (1959).

34. W. L. Bond and J. Andrus, Phys. Rev. 101, 1211 (1956).

35. N. A. Brilliantow and I. W. Obreimow, Phys. Z. Sowjet. 6, 587 (1934).

36. N. A. Brilliantow and I. W. Obreimow, Phys. Z. Sowjet. 12, 7 (1937).

37. J. F. Nye, Proc. Roy. Soc. (London) A198, 190 (1949).

38. B. H. Kear and P. L. Pratt, Acta Met. 6, 457 (1958).

39. S. Mendelson, J. Appl. Phys. 32, 1999 (1961).

40. H. B. Huntington, J. E. Dickey and R. Thomson, Phys. Rev. 100, 1117 (1955).

41. P. L. Pratt, Acta Met. 1, 103 (1953).

42. F. C. Frank and W. T. Read, Phys. Rev. 79, 722 (1950).

43. W. T. Read, Dislocation in Crystal (McGraw-Hill, New York, 1953).

44. G. E. Dieter, Mechanical Metallurgy, 2nd ed. (McGraw-Hill, New York, 1976), p. 187.

45. J. F. Nye, Nature 161, 367 (1948).

46. S. Mendelson, J. Appl. Phys. 32, 1579 (1961).

47. J. W. Dally and W. F. Riley, Experimental Stress Analysis, 2nd ed. (McGraw-Hill, New York, 1978), Chapter 13, p. 407.

48. J. C. Maxwell, Trans. R. Soc. Edinburgh 20, 87 (1853).

49. A. A. Griffith, Phil. Trans. Roy. Soc. (London) A221, 163 (1921).

50. E. Orowan, Weld. J. 34, 1575 (1955).

51. J. Eftis and H. Liebowitz, Eng. Fract. Mech. 7, 101 (1975).

52. A. A. Wells, Bt. Weld. J. 13, 2 (1965).

53. A. A. Wells, Eng. Fract. Mech. 1, 399 (1970).

54. D. Broek, Elementary Engineering Fracture Mechanics, 3rd ed. (Martinus Nijhoff Publishing, The Hague, 1982), Chapter 5, p. 122.

55. J. R. Rice, J. Appl. Mech. 35, 379 (1968).

56. M. Sakai, K. Urashima, and M. Inagaki, J. Am. Ceram. Soc. 66, 868 (1983).

57. J. Nakayama, Japan. J. Appl. Phys. 3, 422 (1964).

58. L. W. Smiser and T. D. McGee, J. Am. Ceram. Soc. 52, 681 (1969).

59. D. B. Williams, Practical Analytical Electron Microscopy in Materials Science (Philips Electronic Instruments, Inc., Mahwah, New Jersey, 1984), Chapter 6, p. 126.

60. J. W. Edington, Practical Electron Microscopy in Materials Science (N. V. Philips Gloeilampenfabrieken, Eindhoven, 1975), Monograph 2, p. 35.

61. R. C. Bradt, D. P. H. Hasselman and F. F. Lange, Fracture Mechanics of Ceramics (Plenum Press, New York, 1974), Vol. 1, p. 42.

62. J. A. Coppola, D. P. H. Hasselman and R. C. Bradt, Am. Ceram. Soc. Bull. 52, 578 (1973).

63. G. A. Cooper, J. Mater. Sci. 12, 277 (1977).

64. J. I. Bluhm, Eng. Frac. Mech. 7, 593 (1975).

65. H. G. Tattersall and G. Tappin, J. Mater. Sci. 1, 296 (1966).

66. J. Nakayama, J. Am. Ceram. Soc. 48, 583 (1965).

67. J. Nakayama, H. Abe and R. C. Bradt, J. Am. Ceram. Soc. 64, 671 (1981).

68. J. Weertman and J. R. Weertman, Elementary Dislocation Theory (The Macmillan Company, New York, 1964), Chapter 5, p. 127.

69. D. Broek, Elementary Engineering Fracture Mechanics, 3rd ed. (Martinus Nijhoff Publishing, The Hague, 1982), Chapter 4, p. 98.

70. G. A. Basset, Phil. Mag. Ser. 8, 1042 (1958).

71. H. Conrad, J. Met. 16, 582 (1964).

72. W. G. Johnston and J. H. Gilman, J. Appl. Phys. 30, 129 (1959).

73. J. M. Baik, J. Kameda and O. Buck, Metallurgica 17, 1443 (1983).

74. M. Inagaki, K. Urashima, S. Toyomasu, Y. Goto and M. Sakai, J. Am. Ceram. Soc. 68, 704 (1985).

ACKNOWLEDGMENTS

The author wishes to express his special gratitude and appreciation to Professor T. D. McGee for his advice, guidance and encouragement during the course of this study.

The author wishes to thank the Department of Materials Science and Engineering for the helpfulness and support in this work.

The author wishes to thank Professors D. R. Wilder, O. Buck, J. D. Verhoeven, B. L. Pierson and M. S. Wechsler for their guidance.

The author also wishes to thank Ms. Barbara Dubberke for the excellent typing of this manuscript.

Finally, I would like to thank my wife, Jing Lan, for her patience and understanding.

APPENDIX A. SEMIQUANTITATIVE SPECTROGRAPHIC ANALYSIS OF SODIUM CHLORIDE SINGLE CRYSTALS

The ingots of sodium chloride single crystals used were obtained from the Harshaw Chemical Company, Solon, Ohio. A semiquantitative spectrographic analysis of samples from three ingots was performed previously by S. A. Long [20]. The following results from Long [20] in Table 3 can be taken as a reference for the ingots used in this research.

Table 3. Semiquantitative spectrographic analysis of Harshaw Chemical Company optical grade NaCl

Ingot	Si (ppm)	Cu (ppm)	Al (ppm)	Mg (ppm)
A	~ 10	< 50	~ 50	< 20
B	~ 10	< 50	< 50	< 20
C	< 10	< 50	< 20	< 20

APPENDIX B. DESIGN OF PYROGENIC SYSTEM

Furnace Insulation

Figure 33 is the furnace used in this research. Because the highest temperature of the furnace is 300°C, the furnace is insulated with fiberfrax.

Some basic parameters for furnace design are listed below.

Inside temperature of the furnace:

$$T_h = 300°C = 572°F.$$

Outside surface temperature of the furnace:

$$T_\ell = 120°F.$$

Room temperature:

$$T_r = 70°F.$$

Thermal conductivity of the fiberfrax:

$$K = 0.048 \ (W/m \cdot °K).$$

The heat losses (per unit area) from the furnace to the surroundings for the condition above:

$$q_{loss} = 100 \ B.T.U./ft^2 \cdot hr. \tag{51}$$

The conduction heat transfer by the insulating material can be written as

$$q_C = KA \frac{\partial T}{\partial x} \tag{52}$$

where

K = thermal conductivity,

Figure 33. The small furnace used in the high temperature tests

A = area and

$\frac{\partial T}{\partial x}$ = temperature gradient.

Equation (52) can be rewritten as

$$q_c/A = K \frac{\partial T}{\partial x} \quad . \tag{53}$$

q_c/A should be equal to q_{loss} of the Eq. (51). From Eq. (53), the thickness of insulating material (Δx) can be obtained

$$\Delta x = 40 \text{ mm} \quad .$$

Power Supply

The outside diameter of the furnace (d) is 0.172 m. The height of the furnace (h) is 0.16 m. And the diameter of force rod (d_1) is 0.06 m. Therefore, the surface area of the furnace is

$$S_{furnace} = \pi dh + 2 \cdot \pi(\frac{d}{2})^2 - 2 \cdot \pi(\frac{d_1}{2})^2$$

$$= 0.14 \ (m^2) \quad . \tag{54}$$

The heat losses by the furnace surface can be written as

$$W_f = q_{loss} \times S_{furnace} = 44 \text{ (watts)} \quad . \tag{55}$$

The heat losses by the force rod are given by

$$q_r = K_r A_r \frac{\partial T}{\partial x} \tag{56}$$

where K_r is the thermal conductivity of the force rod (20 w/m · °K) and A_r is the top surface area of the force rod. The q_r calculated from Eq. (56) was 236 watts. The total heat losses by the two force rods are

$$W_r = 2 \times q_r = 472 \text{ (watts)} \quad . \tag{57}$$

Equation (55) gives the heat losses by the furnace surface. Equation (57) gives the heat losses by the force rods. Therefore, the power supply should be the sum of the Eqs. (55) and (57):

$$W = W_f + W_r = 516 \text{ (watts)} \quad .$$

Other sources of heat losses are possible. For example, heat convection through the gap between the furnace and the force rod. We wanted the furnace to reach the maximum temperature (300°C) as soon as possible. Hence, a power supply of 800 watts was selected. The voltage was controlled by a transformer. The maximum voltage was 60 V. The maximum current was 13 A. "Kanthal" A strip was used as the heating element.